INFORMATION TO USERS

This manuscript has been reproduced from the microfilm master. UMI films the text directly from the original or copy submitted. Thus, some thesis and dissertation copies are in typewriter face, while others may be from any type of computer printer.

The quality of this reproduction is dependent upon the quality of the copy submitted. Broken or indistinct print, colored or poor quality illustrations and photographs, print bleedthrough, substandard margins, and improper alignment can adversely affect reproduction.

In the unlikely event that the author did not send UMI a complete manuscript and there are missing pages, these will be noted. Also, if unauthorized copyright material had to be removed, a note will indicate the deletion.

Oversize materials (e.g., maps, drawings, charts) are reproduced by sectioning the original, beginning at the upper left-hand corner and continuing from left to right in equal sections with small overlaps.

Photographs included in the original manuscript have been reproduced xerographically in this copy. Higher quality 6" x 9" black and white photographic prints are available for any photographs or illustrations appearing in this copy for an additional charge. Contact UMI directly to order.

ProQuest Information and Learning
300 North Zeeb Road, Ann Arbor, MI 48106-1346 USA
800-521-0600

UMI®

Reproduced with permission of the copyright owner. Further reproduction prohibited without permission.

Reproduced with permission of the copyright owner. Further reproduction prohibited without permission.

SELF-ASSEMBLY OF DITHIOL MONOLAYERS ON AU(111)

ALLAN MACDAIRMID

OCTOBER 2001

A THESIS SUBMITTED IN PARTIAL FULFILLMENT OF THE REQUIREMENTS OF THE MASTER OF SCIENCE DEGREE IN PHYSICS

LAKEHEAD UNIVERSITY
THUNDER BAY, ONTARIO
CANADA

Reproduced with permission of the copyright owner. Further reproduction prohibited without permission.

National Library of Canada
Acquisitions and Bibliographic Services
395 Wellington Street
Ottawa ON K1A 0N4
Canada

Bibliothèque nationale du Canada
Acquisitions et services bibliographiques
395, rue Wellington
Ottawa ON K1A 0N4
Canada

Your file Votre référence

Our file Notre référence

The author has granted a non-exclusive licence allowing the National Library of Canada to reproduce, loan, distribute or sell copies of this thesis in microform, paper or electronic formats.

The author retains ownership of the copyright in this thesis. Neither the thesis nor substantial extracts from it may be printed or otherwise reproduced without the author's permission.

L'auteur a accordé une licence non exclusive permettant à la Bibliothèque nationale du Canada de reproduire, prêter, distribuer ou vendre des copies de cette thèse sous la forme de microfiche/film, de reproduction sur papier ou sur format électronique.

L'auteur conserve la propriété du droit d'auteur qui protège cette thèse. Ni la thèse ni des extraits substantiels de celle-ci ne doivent être imprimés ou autrement reproduits sans son autorisation.

0-612-64725-0

Canada

Reproduced with permission of the copyright owner. Further reproduction prohibited without permission.

Self-Assembly of Dithiol Monolayers on Au(111)

by

Allan MacDairmid

Abstract

This thesis compares the self-assembly of octanethiol, a representative n-alkanethiol, with dithiothreitol (DTT) on Au(111). Octanethiol is an eight carbon n-alkanethiol while DTT is a four carbon α,ω dithiol with hydroxyl groups on the second and third carbons. We find that octanethiol forms a densely packed c(4×2) superlattice of the $(\sqrt{3}\times\sqrt{3})R30°$ structure characteristic of n-alkanethiols. DTT forms a less dense monolayer, possibly $c(2\sqrt{3}\times\sqrt{3})$. Both monolayers exhibit pits 2.5 Å deep equivalent to the height of one gold layer. The time evolution of pitting is investigated in both systems using scanning tunneling microscopy (STM). The fraction of the surface that is covered by these pits is found to be in the range of 0.05-0.10 for both systems and consistent with previous n-alkanethiol studies. The mean pit radius approaches an equilibrium value of ~19 Å for both thiol species. It has been observed that DTT modified systems do not reach this equilibrium value as quickly as octanethiol modified systems. The nature of the binding of DTT to gold is also investigated using STM and Auger electron spectroscopy (AES) studies. AES studies involving Ellman's Reagent, a marker species, suggest that a significant fraction of the DTT binds to the gold surface via two Au-S bonds.

Reproduced with permission of the copyright owner. Further reproduction prohibited without permission.

Acknowledgements

There are many people that deserve thanks for the help that they provided me during my research. My supervisor, Mark Gallagher, taught me many things about the techniques that I used to investigate SAMs and even more about the research process in general.

I would also like to thank Jeff Banks, Christine Gottardo, and Robert Lennox for answering my numerous chemistry related questions about the molecules that I was using. Marie Cappello and Karen Hardy showed me how to prepare thiol solutions and deal with resulting sulphur odours. Todd Keeler performed the film thickness measurements.

At this time, I would also like to thank the Natural Science and Engineering Research Council for supporting me during my time at Lakehead University through the Undergraduate Student Research Assistantship Program and the Post-Graduate Scholarship Program.

Reproduced with permission of the copyright owner. Further reproduction prohibited without permission.

Table of Contents

Reproduced with permission of the copyright owner. Further reproduction prohibited without permission.

Introduction

Reproduced with permission of the copyright owner. Further reproduction prohibited without permission.

Self-assembled monolayers (SAMs) have received a great deal of attention over the past decade. The most commonly studied system has been n-alkanethiol, $CH_3(CH_2)_{n-1}SH$, adsorption onto Au(111) substrates. The SAM that forms from adsorption is a compact layer that exhibits molecular order. Once formed, a simple n-alkanethiol SAM can be modified to tailor the chemical properties of the surface. This includes the wetting, chemical specificity, and electronic characteristics of the film. As a wider understanding of self-assembly is attained, more and more complicated molecules can be incorporated into the surface layer.

This thesis discusses the properties of SAMs of aliphatic thiols. Octanethiol is studied as a representative n-alkanethiol and compared with dithiothreitol (DTT), a functionalized dithiol molecule. The chemical structure of octanethiol and DTT is shown in Figure 1. The effect of the presence of a second sulphydryl group and two hydroxyl groups on the self-assembly of DTT will be observed using scanning tunneling microscopy (STM) and Auger electron spectroscopy (AES) and compared with the self-assembly of the more conventional octanethiol.

For the first time, molecular images of DTT were obtained indicating a

Reproduced with permission of the copyright owner. Further reproduction prohibited without permission.

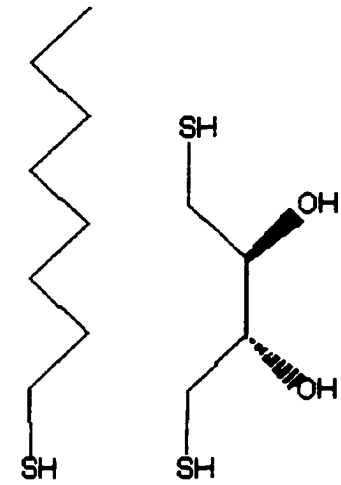

Figure 1. Structural diagram of octanethiol (left) and dithiothreitol (right).

larger unit cell than octanethiol. Auger results suggest sulphur is present in similar quantities for both octanethiol and dithiothreitol and use of Ellman's reagent suggests both sulphur atoms bind the DTT to the gold. These results suggest a $(2\sqrt{3}\times\sqrt{3})$ lattice for DTT. Investigations into the degree of surface pitting suggest that both dithiothreitol and octanethiol, while chemically very different, seem to trigger pitting via the same mechanism. At 60°C, DTT modified films appear to reach the same equilibrium pit radius as octanethiol.

A discussion of the main issues surrounding SAMs is provided, followed by sections outlining the experimental techniques involved in observing and preparing SAMs. Observations concerning the ordering of the two SAMs are

Reproduced with permission of the copyright owner. Further reproduction prohibited without permission.

presented along with the results of a study on the time evolution of pitting. Finally, a summary discussion of the results is presented and future investigations are suggested.

Reproduced with permission of the copyright owner. Further reproduction prohibited without permission.

Self-Assembled Monolayers

Reproduced with permission of the copyright owner. Further reproduction prohibited without permission.

Single molecular monolayers have been utilized in technological applications for several decades dating back to the 1930's[1]. Monolayers of amphiphilic molecules comprised of both hydrophilic and hydrophobic moieties were used to coat metals and control the condensation properties of water inside steam engines[2]. Uncoated metals resulted in a complete layer of water condensation which then insulated the condenser from accumulating more steam. The presence of an amphiphilic monolayer triggered water to condense as droplets and subsequently fall off. The droplet formation facilitated the condensation of larger quantities of steam and increased heat conversion efficiency by over 200 %. Researchers realized that the amphiphiles were bound to the surface by a metallophillic head group and that the hydrocarbon tails of the molecules aligned and formed the layer on which steam droplets could condense. In the late 1950's, scientists investigated droplet condensation on monolayers of alkanethiols on copper surfaces[3]. By the early 1980's, alkyl disulfide monolayers were being studied on gold substrates[4].

While early research focussed on controlling wetting properties, more recent studies have investigated applications in biochemical sensing[5], biomimetics[6], and nanoengineering[7]. For example, SAMs can be altered on a

Reproduced with permission of the copyright owner. Further reproduction prohibited without permission.

molecule by molecule basis using the tip of a scanning probe microscope as a local catalyst[8]. This allows for design in the nanometre scale regime.

While there are many different classes of SAMs (alkyl trichlorosilanes on SiO_2, organic acids on mica, etc) the primary focus of SAM research has been on alkyl thiols on Au(111). Alkyl thiols are robust molecules that are not moisture sensitive like alkyl trichlorosilanes and Au(111) provides a crystalline surface that allows SAM crystallization studies to be conducted[9]. Another benefit of using Au(111) as the substrate is that gold does not oxidize readily in air so scanning probe microscopy investigations of alkyl thiol SAMs can be performed in ambient conditions. This discussion will only consider SAMs of alkanethiol molecules and their derivatives on Au(111) substrates.

Au(111)

Metallic gold arranges itself in a face-centred cubic (fcc) lattice with a lattice constant of 4.08 Å[10]. The fcc unit cell can be thought of as a cube with eight atoms situated at the eight vertices, (0,0,0), (1,0,0), (0,1,0), (0,0,1), (1,1,0), (0,1,1), (1,0,1), and (1,1,1), and six more atoms occupying the centres of the six faces, $(0,\frac{1}{2},\frac{1}{2})$, $(\frac{1}{2},0,\frac{1}{2})$, $(\frac{1}{2},\frac{1}{2},0)$, $(1,\frac{1}{2},\frac{1}{2})$, $(\frac{1}{2},1,\frac{1}{2})$, and $(\frac{1}{2},\frac{1}{2},1)$, as shown in Figure 2. When the unit cells are repeated to generate the lattice, each of the

Reproduced with permission of the copyright owner. Further reproduction prohibited without permission.

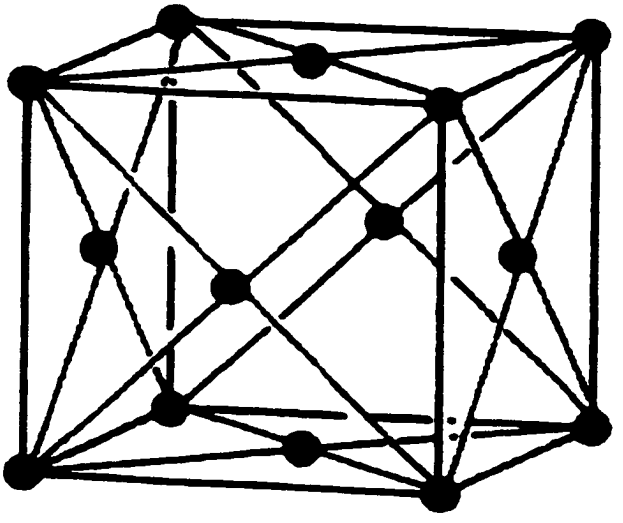

Figure 2. Unit cell of face-centred cubic (fcc) lattice[10].

eight corner atoms sit partially in eight cells thereby contributing one eighth of an atom to each unit cell. Each of the six face atoms are shared by only two unit cells so they contribute one half of an atom to each unit cell. Analysing the unit cell in this manner yields four atoms per unit cell. Fcc crystals exhibit close packing which, using a hard sphere model, yields a packing density of 0.74[10]. This is the highest packing fraction possible.

The (111) plane of the crystal passes through the atoms at positions (0,0,1), (1,0,0), (0,1,0), $(0,\frac{1}{2},\frac{1}{2})$, $(\frac{1}{2},0,\frac{1}{2})$, and $(\frac{1}{2},\frac{1}{2},0)$ forming a hexagonal lattice as shown in Figure 3. The nearest neighbour spacing in the (111) plane is $2^{-\frac{1}{2}}$ times the lattice constant or α=2.88 Å. Because the lattice vectors define a

Reproduced with permission of the copyright owner. Further reproduction prohibited without permission.

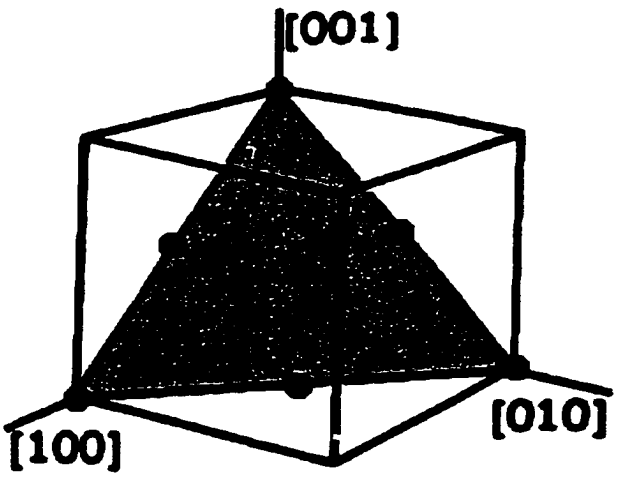

Figure 3. (111) plane of an fcc crystal[10].

cube, the [111] vector is normal to the (111) plane. It should be emphasized that this does not hold true for non-cubic crystals.

The (111) plane can be thought of as a sheet of densely packed hard spheres as shown in Figure 4. Because the (111) plane is clase packed, it is the low energy plane of the crystal. Starting with a single layer of close packed atoms, the second layer can be stacked on top of the first by placing spheres at

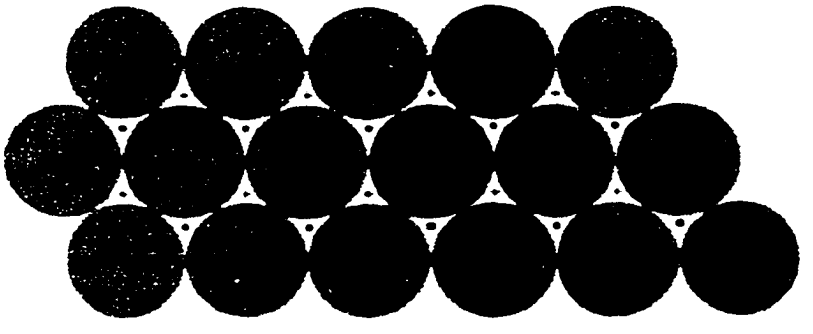

Figure 4. Possible stacking sites for a close packed lattice[10].

Reproduced with permission of the copyright owner. Further reproduction prohibited without permission.

B sites. The third layer can sit at the unused C sites or revert back to the original A sites. ABC stacking corresponds to fcc crystals while ABA stacking corresponds to hexagonal close packed (hcp) crystals.

Herringbone Reconstruction

Crystalline surfaces often undergo reconstruction to reduce the energy of the surface layer. This occurs because atoms in the surface layer do not have as many nearest neighbours as those in the bulk crystal. The surface layer of (111) terminated gold crystals reduces its energy by incorporating one extra atom into every ($23\alpha \times \sqrt{3}\alpha$) cell, where α is the gold spacing within the (111) plane. This results in a 4.4 % increase in areal density[11]. The reconstruction realizes this excess by periodically changing from the ABC stacking of fcc crystals to the faulted ABA stacking of hcp crystals[12] as shown in Figure 5. At phase boundaries, the surface layer buckles because the atoms are forced to

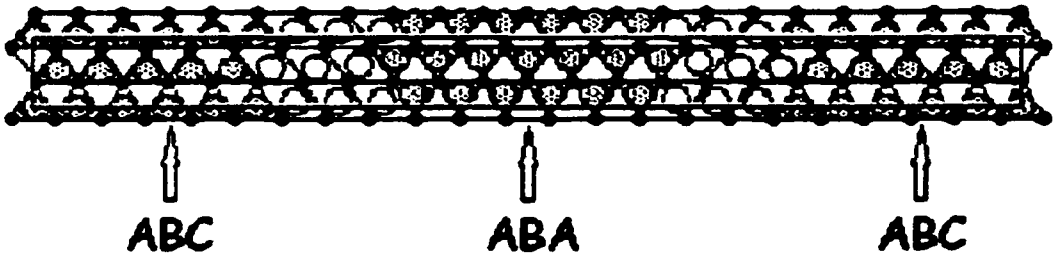

Figure 5. Top view of the ($23 \times \sqrt{3}$) cell of the herringbone reconstruction showing bridge site phase boundaries (white circles) between ABC stacking and faulted ABA stacking[11].

Reproduced with permission of the copyright owner. Further reproduction prohibited without permission.

occupy bridge sites of the second layer due to the transition from C hollow sites to A hollow sites. It should be emphasized that the increased areal density is accommodated by the surface buckling and that there is no change in the lattice constant of the fcc and hcp regions. The energy tied up in having atoms occupy bridge sites is compensated by having the rest of the atoms occupy A and C hollow sites. The energy difference between fcc and hcp stacking can be determined by comparing the relative domain size in the (23×√3) cell. When the reconstruction is observed with STM, parallel pairs of ridges (white circles in Figure 5) are seen zigzagging across the surface. The atoms that occupy bridge sites protrude 0.15 Å above the other surface atoms that occupy hollow sites as predicted using a hard sphere model and verified experimentally by helium scattering. The periodicity of the (23×√3) cell is 23α or ~66 Å as measured using scanning tunneling microscopy[12].

SAM Formation and Packing

Alkanethiol SAMs form as a result of the strong affinity between sulphur and gold. The thiol head groups form strong covalent bonds with the gold substrate and the hydrocarbon backbone of the molecules align and stabilize the monolayer via van der Waals interactions. A typical dense packed

Reproduced with permission of the copyright owner. Further reproduction prohibited without permission.

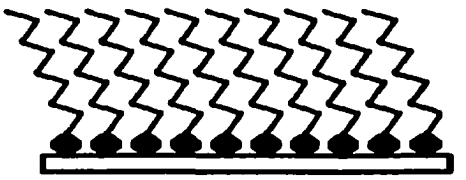

Figure 6. Dense packed SAM of n-alkanethiol on Au(111) (n=8).

SAM is shown in Figure 6. It has been observed that SAM formation is possible from both liquid and gas phase deposition[11]. While liquid phase deposition is the most common technique used, gas phase deposition removes solvent effects from the system. This is of significance when the alkanethiol is functionalized.

Systems involving the self-assembly of n-alkanethiols of varying lengths

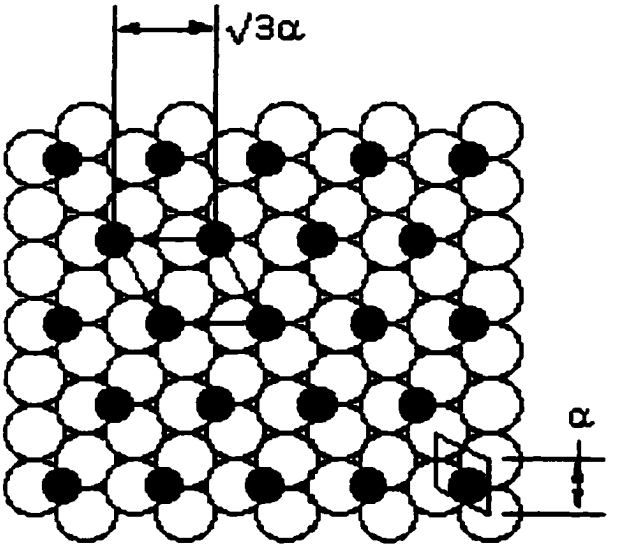

Figure 7. Commensurate (√3×√3)R30° lattice of n-alkanethiol (dark circles) on Au(111) substrate (open circles) (α=2.88 Å).

Reproduced with permission of the copyright owner. Further reproduction prohibited without permission.

ranging from eight to twenty carbon atoms attain a commensurate ($\sqrt{3}\times\sqrt{3}$) lattice rotated by 30° with respect to the substrate lattice vectors as shown in Figure 7[13]. The SAM lattice results in a periodicity of $\sqrt{3}\alpha$ or 5.00 Å along both lattice directions. It has also been determined from IR studies that the hydrocarbon backbone is tilted ~30° with respect to the surface normal and that there are two distinct planes defined by the all-trans hydrocarbon backbone[14]. A c(4×2) superlattice of the adsorbed n-alkanethiol has been observed that is believed to be caused by the pairing of the two different all-trans planes[15] as shown in Figure 8. The c(4×2) superlattice results in the

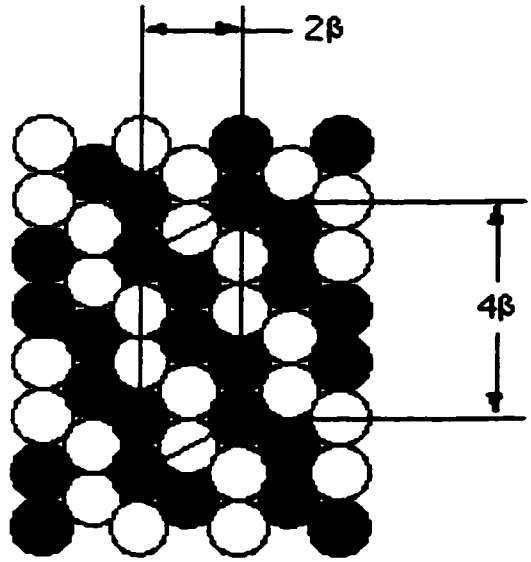

Figure 8. c(4×2) superlattice of n-alkanethiol SAMs arising from the two different orientations of the all-trans planes of the molecules (β=5.00 Å).

Reproduced with permission of the copyright owner. Further reproduction prohibited without permission.

densest possible packing observed with a molecular area of 21.6 Å^2. Recently, another densely packed (6×√3) phase was observed on an octanethiol modified film after being stored for six months at room temperature (RT)[16]. Complete monolayer coverage is attained using 1 mM concentrations of alkanethiol for a relatively small (1 cm^2) Au(111) sample.

Other phases of SAMs have been observed for smaller chain length alkanethiols and longer chain length molecules at low coverages. These phases, often called the "pinstripe phases" consist of molecules lying down on the surface to form a (p×√3) lattice where p is an integer that depends on the length of the thiol molecule[17]. The molecules align head to head, and subsequently, tail to tail to form stripes along the surface.

Temperature Effects

Alkanethiol SAMs form when modified at RT. The resulting monolayer is ordered but exhibits depressions in the surface equivalent to a gold single atomic step height (2.5 Å)[18]. The threefold symmetry of the surface results in boundaries between domains with different tilt directions. Heating the surface to 50°C increases the average domain size. At 100°C, the mobility of gold atoms in the surface layer increases and the depressions begin to fuse with

Reproduced with permission of the copyright owner. Further reproduction prohibited without permission.

step edges. Above 100°C, some thiol molecules evaporate from the surface resulting in striped depressions where thiol molecules are no longer present. The monolayer can remain crystalline with as little as 25 % of the saturation c(4×2) density. This is attributed to the fact that the molecules can diffuse through the monolayer faster than the evaporation process can remove them so the monolayer can heal itself. As the temperature is increased further, the desorption rate increases and the monolayer rapidly degrades until it is completely gone at 130°C.

Reproduced with permission of the copyright owner. Further reproduction prohibited without permission.

Experimental Techniques

Reproduced with permission of the copyright owner. Further reproduction prohibited without permission.

Scanning Tunneling Microscopy

Scanning tunneling microscopy (STM) is the primary technique employed in this study of self-assembly. STM is a scanning probe technique used for obtaining real space information about surfaces on the atomic scale. The first functional STM was realized in 1981 by Binning, Rohrer, and Gerber[19]. The potential of STM was demonstrated in 1982 with the publication of images of the (7×7) reconstructed surface of Si(111). The structure of the reconstructed surface had been debated for over twenty years. The unit mesh comprised 49 atoms which made analysis based on diffraction experiments very difficult. Several models were proposed but comparison between the STM results and theoretical predictions confirmed the dimer-adatom-stacking-fault model[20]. The ability to observe atomic scale features on surfaces with STM led to the wide-scale use of STM as a surface science technique and the awarding of the Nobel prize for physics to Binnig and Rohrer in 1986. STM depends on the relatively simple physical phenomenon of quantum tunneling.

Quantum Tunneling

Quantum tunneling arises when a particle is incident on a finite potential barrier with insufficient energy to overcome it[21]. Though classically forbidden,

Reproduced with permission of the copyright owner. Further reproduction prohibited without permission.

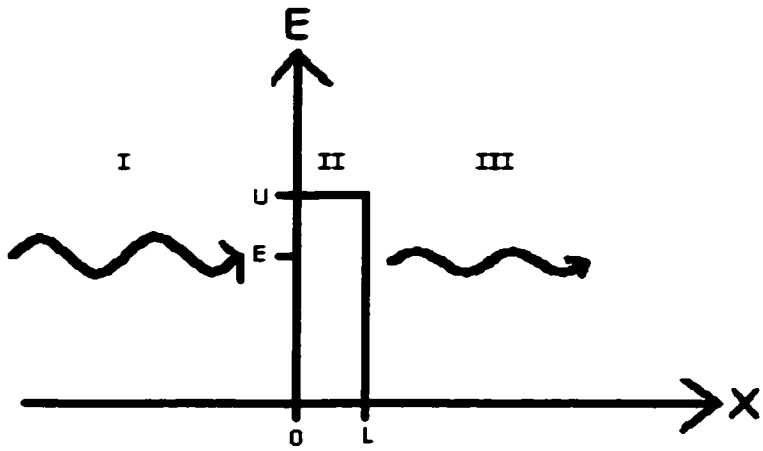

Figure 9. Idealized schematic of quantum tunneling through a finite potential barrier.

there is a non-zero probability that the particle will tunnel through the barrier and emerge on the other side. This phenomenon can easily be demonstrated in one dimension by exploring a system where a free particle with energy, E, is incident on a rectangular potential barrier of width, L, and height, U, starting at x=0 as shown in Figure 9. In region I and III, the wave vector is k and in region II the inverse decay length is κ. The two constants are given by:

$$k = \frac{\sqrt{2mE}}{\hbar}$$

$$\kappa = \frac{\sqrt{2m(U-E)}}{\hbar}$$

The tunneling probability can be expressed as the ratio of the transmitted and

Reproduced with permission of the copyright owner. Further reproduction prohibited without permission.

incident current densities of the particle[19]. Given the current density operator:

$$j_n = -\frac{i\hbar}{2m}\left[\psi_n^* \frac{d\psi_n}{dx} - \psi_n \frac{d\psi_n^*}{dx}\right]$$

the transmitted current density, j_t, the incident tunnel current, j_i, and the tunneling probability, T, are[19]:

$$j_t = \frac{\hbar k}{m}|D|^2$$
$$j_i = \frac{\hbar k}{m}$$
$$T = \frac{j_t}{j_i} = |D|^2$$

Therefore, the tunneling probability is the fraction of incident particles that pass through the barrier, $|D|^2$. At the boundaries of the potential barrier, x=0 and x=L, the wave functions must be continuous since the barrier is finite. Hence the wave functions and their derivatives must equal each other at the boundaries. Applying these boundary conditions yields four equations with four unknowns which can be solved to yield the tunneling probability[22]:

$$T = \frac{4k^2\kappa^2}{(k^2+\kappa^2)^2 \sinh^2(\kappa L) + 4k^2\kappa^2}$$

The tunneling probability can be approximated assuming $\kappa L \gg 1$:

Reproduced with permission of the copyright owner. Further reproduction prohibited without permission.

$$T \approx \frac{16k^2\kappa^2}{(k^2+\kappa^2)^2} e^{-2\kappa L}$$

The tunneling probability is dominated by the exponential term which depends on the effective barrier height, (U-E) which is expressed in κ, and the width, L, of the barrier. Typical tunneling conditions result in a 10-fold increase in the tunneling probability for a 1 Å decrease in barrier width[19].

Since STM relies on the quantum tunneling effect, it is very sensitive to changes in the barrier between the sample and the tip. The tunneling current between the tip and the sample will cancel the tunneling current between the sample and the tip unless a bias is applied to favour tunneling towards the tip or the sample.

The previous treatment provides the exponential dependence of the tunnel current on the tunnel gap thickness, however, it does not consider the structural effects contributed by the tip and the sample. Assuming that the bias voltage that is applied is small, only electrons near the Fermi levels of the tip and the sample can contribute to the tunnel current. A precise determination of the tunnel current is often intractable for realistic tip and sample systems. If a weak coupling between the tip and the sample is assumed,

Reproduced with permission of the copyright owner. Further reproduction prohibited without permission.

the tunnel current can be calculated using first-order perturbation theory[20]:

$$I = \frac{2\pi e}{\hbar}\sum_{m,n}\left\{f(E_m)\left[1-f(E_n)\right]-f(E_n)\left[1-f(E_m)\right]\right\}\left|M_{mn}\right|^2\delta(E_n+eV-E_m)$$

Here f(E) is the Fermi function and M_{mn} is the tunneling matrix element between tip states m and sample states n.

As an approximation, the Fermi functions can be treated as unit step functions. This coupled with the small voltage assumption simplifies the tunnel current expression to:

$$I = \frac{2\pi}{\hbar}e^2V\sum_{m,n}\left|M_{mn}\right|^2\delta(E_m-E_F)\delta(E_n-E_F)$$

In the weak coupling limit, the tunneling matrix element can be determined by integrating the current density operator over any surface inside the tunnel barrier[23]:

$$M_{mn} = -\frac{\hbar^2}{2m}\int\left(\psi_m^*\vec{\nabla}\psi_n-\psi_n\vec{\nabla}\psi_m^*\right)\bullet d\vec{S}$$

In order to calculate the tunneling matrix elements, the wave functions that describe the tip and the sample must be determined. Given the difficulties manufacturing atomically similar tips, the exact structure can not

Reproduced with permission of the copyright owner. Further reproduction prohibited without permission.

be modelled. However, a good approximation can be made by treating the tip as a spherically symmetric current source:

$$\psi_m = \frac{1}{\sqrt{\Omega_t}} \frac{c_t \kappa R e^{\kappa R}}{\kappa |\bar{r} - \bar{r}_0|} e^{-\kappa |\bar{r} - \bar{r}_0|}$$

Here Ω_t is the tip volume, c_t is the normalization coefficient, κ is the inverse decay length for the wave function in vacuum, and R is the radius of curvature of the tip centred at $\bar{r}_0$. The sample wave function can be obtained using a Bloch wave treatment:

$$\psi_n = \frac{1}{\sqrt{\Omega_s}} \sum_G a_G e^{-\left(\kappa^2 + |\bar{k}_{||} + \bar{G}|^2\right)^{1/2} z} e^{i(\bar{k}_{||} + \bar{G}) \cdot \bar{x}}$$

Here Ω_s is the sample volume, a_G is the Fourier coefficient, κ is the inverse decay length far the wave function in vacuum, $\bar{k}_{||}$ is the surface Bloch wave vector of the state, and $\bar{G}$ is the reciprocal lattice vector.

Substituting the tip and sample wave functions into the expression for the tunneling matrix elements gives:

$$M_{mn} = \frac{\hbar^2}{2m} \frac{4\pi}{\kappa} \frac{\kappa R}{\sqrt{\Omega_t}} e^{\kappa R} \psi_n(\bar{r}_0)$$

The significance of this result is that the tunneling matrix elements depend on

Reproduced with permission of the copyright owner. Further reproduction prohibited without permission.

the value of the wave function of the sample at the position of the centre of curvature of the tip. With the tunneling matrix element determined the tunnel current can be calculated:

$$I \propto \sum_n |\psi_n(\vec{r}_0)|^2 \delta(E_n - E_F) = \rho(\vec{r}_0, E_F)$$

Hence the tunnel current is directly proportional to the local density of states (LDOS) near the Fermi level at the position of the tip. This model assumes that the tunneling barrier is a vacuum. It is not clear how the presence of an adsorbed layer within the barrier would affect tunneling.

Operating Principles

One of the major implications of STM is that it does not need to be operated in a vacuum environment[19]. The barrier between the tip and the sample is so small (< 1 nm) that an ambient STM can still function properly. Ambient STM requires that the system being imaged is stable in atmospheric conditions. This is not often the case since many conducting surfaces oxidize quickly. For these surfaces, Ultrahigh vacuum STM is necessary.

The most significant technological development that led to the successful implementation of STM was the realization that piezoelectric ceramics,

Reproduced with permission of the copyright owner. Further reproduction prohibited without permission.

materials that change their shape in the presence of an applied electric field, can be controlled with atomic scale precision[19]. Typically, the resulting length changes are several Å/V at RT. The scanning tip is attached to a set of piezoelectric ceramics which are manipulated by control electronics to obtain motion in all three dimensions.

Scanning tunneling microscopes are most cammonly operated in constant current mode. In this mode, a constant tunnel current (J_T) is maintained for a given bias (V_T) while it is raster scanned across the sample by ceramics P_x and P_y as shown in Figure 10[20]. To maintain a constant current while scanning, the tip is moved toward or away from the surface by changing the piezo voltage (V_p) to induce a change in the length of the ceramic P_z. A computer (CU) is used to collect the height variations as a function of x and y and the resulting image is

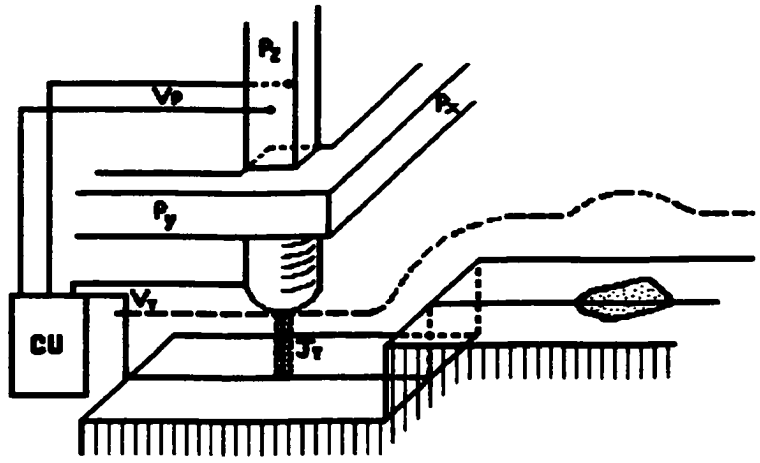

Figure 10. Schematic diagram of STM in constant current mode[20].

Reproduced with permission of the copyright owner. Further reproduction prohibited without permission.

displayed using a colour gradient.

An atomic resolution image of highly orientated pyrolytic graphite (HOPG) obtained using constant current imaging is shown in Figure 11. The gray, white, and black regions of the image correspond to open, overlapping, and dark circles respectively in the stacking diagram. This example demonstrates the sensitivity of the tunnel current to changes in the LDOS. Surface layer atoms sitting directly on top of second layer atoms appear higher in the image because of the extra electron density contributed from the second layer atom. Figure 11 also demonstrates the high degree of spatial resolution possible with an STM.

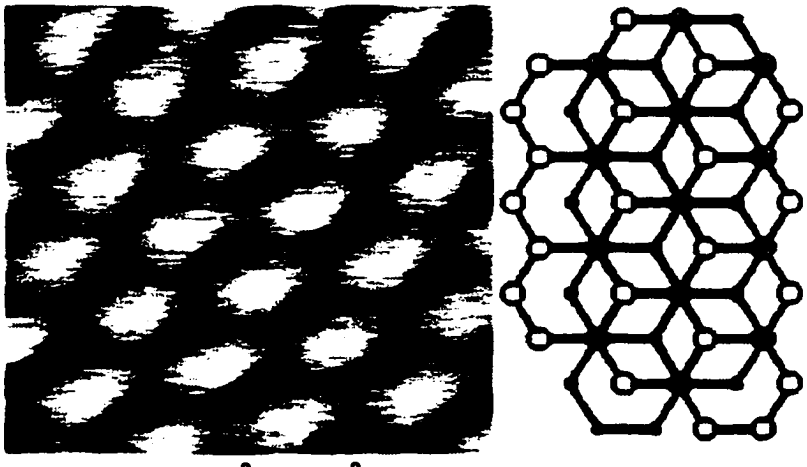

Figure 11. 10Å × 10 Å atomic resolution image of HOPG (left) and stacking diagram for top two layers (right). (Δz=1.2 Å) Tunneling conditions: +0.4 V and 1.0 nA.

Reproduced with permission of the copyright owner. Further reproduction prohibited without permission.

Instrumentation

The STM that is used in the lab is an RHK Technology "Besocke" style scan head controlled by RHK Technology SPM 100 electronics. The scanning tip is a fine wire of platinum-rhodium alloy (7:3) and it sits inside a single scan tube. The tip is prepared by cutting the wire at an angle and, at the same time, pulling out to draw the wire to a point. The scan tube consists of a cylindrical piezoelectric ceramic comprised of four outer electrodes. The inside of the scan tube is grounded. Applying a voltage across one of the quadrants will result in the tube thinning and becoming longer in that quadrant. If the opposing quadrant is not given the same bias, the ceramic will bend due to the length difference between the two sides. In this manner the tip can be manipulated to move in x or y. A uniform voltage applied to all four quadrants causes the whole ceramic to elongate and move the tip in z.

In order to get the scan tip into tunneling range, it is necessary to have a course approach mechanism that will bring the tip into close proximity with the surface without crashing it. This is achieved with the use of three tubes (legs) similar to the scan tube that are located 120° apart as shown in Figure 12. The legs are lowered onto a three segment circular ramp. A sawtooth waveform is

Reproduced with permission of the copyright owner. Further reproduction prohibited without permission.

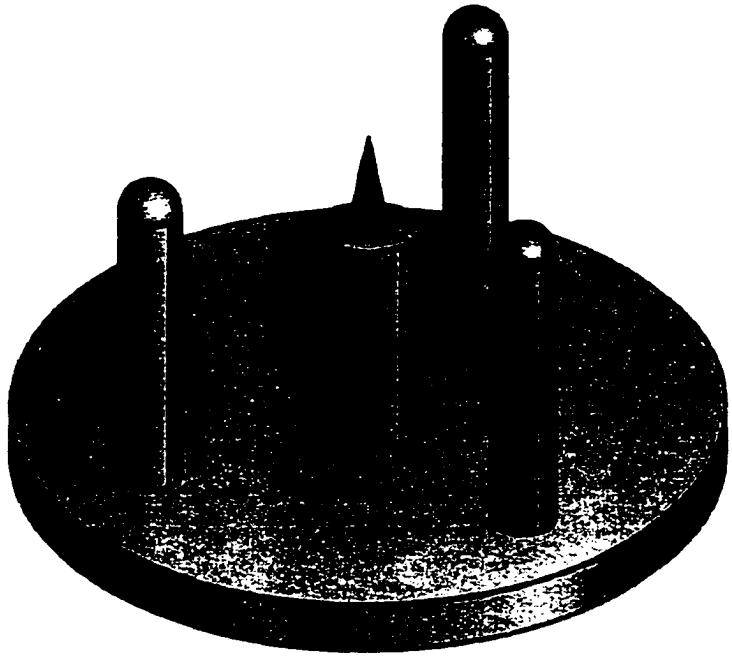

Figure 12. "Besocke" STM scan head with three walking legs and central scan tube[24].

applied to the legs to make them bend tangent to the circular ramp and then quickly straighten[24]. This jerking "stick, slip" motion causes the legs to walk the scan head down the ramp. To prevent the tip from crashing into the surface, the control electronics use the feedback circuitry mentioned earlier. The software generates a false tunnel current to fool the electronics into thinking the STM has crashed. The feedback electronics then fully retract the tip. Once the legs have "stepped", the feedback moves the tip toward the surface and tries to detect a real tunnel current. If no current is detected, the cycle repeats and the STM walks down the ramp.

Reproduced with permission of the copyright owner. Further reproduction prohibited without permission.

Auger Electron Spectroscopy

Another technique used to monitor the presence of thiol molecules on the surface is Auger electron spectroscopy (AES). AES measures the energy of electronic transitions in core level atoms to provide insight into the elemental composition of the surface under study[25]. The basic premise of AES is as follows. An incident particle knocks a core level electron out of an atom leaving a vacancy. The vacancy is filled by an electron from a higher energy level and, to conserve energy, a third electron is excited as shown in Figure 13. If the emitted electron has sufficient energy to escape the atom, its kinetic energy

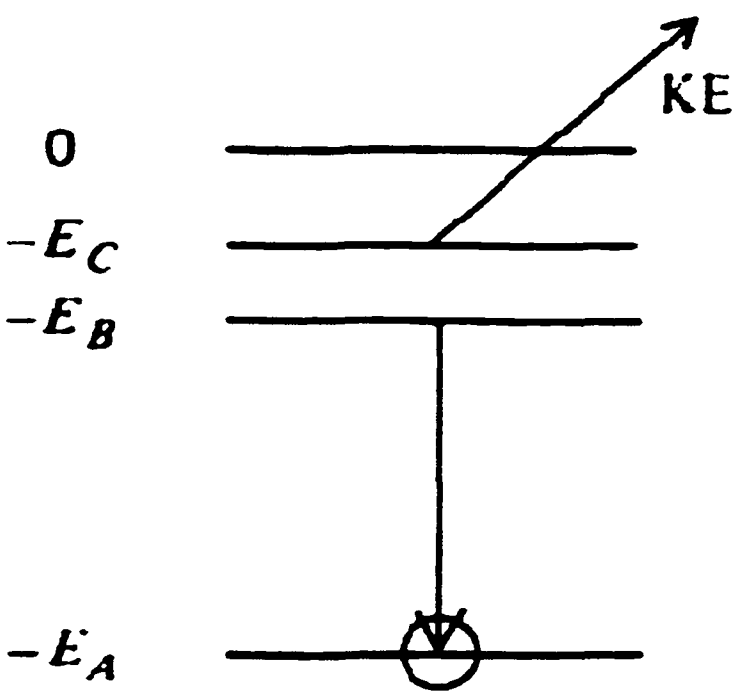

Figure 13. Energy level diagram of Auger electron emission[25].

Reproduced with permission of the copyright owner. Further reproduction prohibited without permission.

will equal the difference between the energy levels involved ($KE=E_A-E_B-E_C+U_{BC}$) where U_{BC} is the interaction energy of the final two hole state of the atom[26]. This emitted electron, called an Auger electron, is collected and analysed to provide information about the atom that it came from. The energy of the emitted Auger electron is characteristic of the element that it came from and, subsequently, each element yields a characteristic spectrum. AES must be performed in an ultrahigh vacuum (UHV) chamber to ensure the unimpeded transit of Auger electrons from the sample to the detector.

Operating Principles

The spectrometer fires a beam of electrons at the sample surface and Auger electrons that escape from the surface are counted. The analyser that the electrons pass through uses electric, and sometimes magnetic, fields to select the energy of the Auger electrons. The number of electrons as a function of energy can then be determined.

The beam of electrons fired at the surface is more than adequate to penetrate deep into the surface. However, the kinetic energy of the electrons that escape the surface is typically in the range where the electrons only have a mean free path of a few atomic layers (10 to 500 eV) as shown in Figure 14[27].

Reproduced with permission of the copyright owner. Further reproduction prohibited without permission.

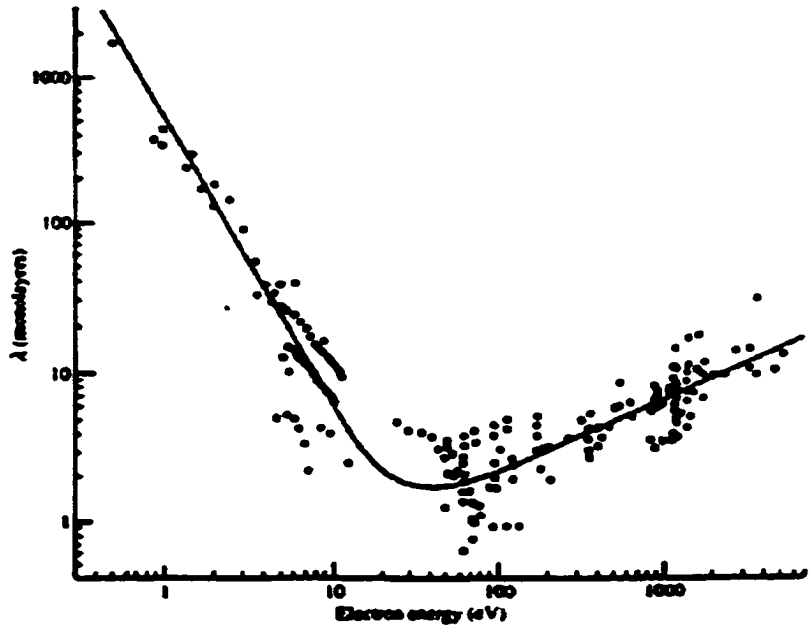

Figure 14. The universal curve of electron mean free path (λ) versus energy[27].

The mean free path as a function of energy is largely material independent and the curve shown in Figure 14 was obtain using a range of elements. The attenuation of electrons from deeper within the sample means that AES is very sensitive to the first few layers of the surface and provides very little information about the bulk of the sample. Since Auger emission is a three electron process, hydrogen and helium can not be detected by AES.

An Auger spectra of Au(111) is shown in Figure 15. To improve the signal to noise ratio of the technique, the derivative of the signal, or electron flux, is measured using a lock-in amplifier. This also improves peak identification since

Reproduced with permission of the copyright owner. Further reproduction prohibited without permission.

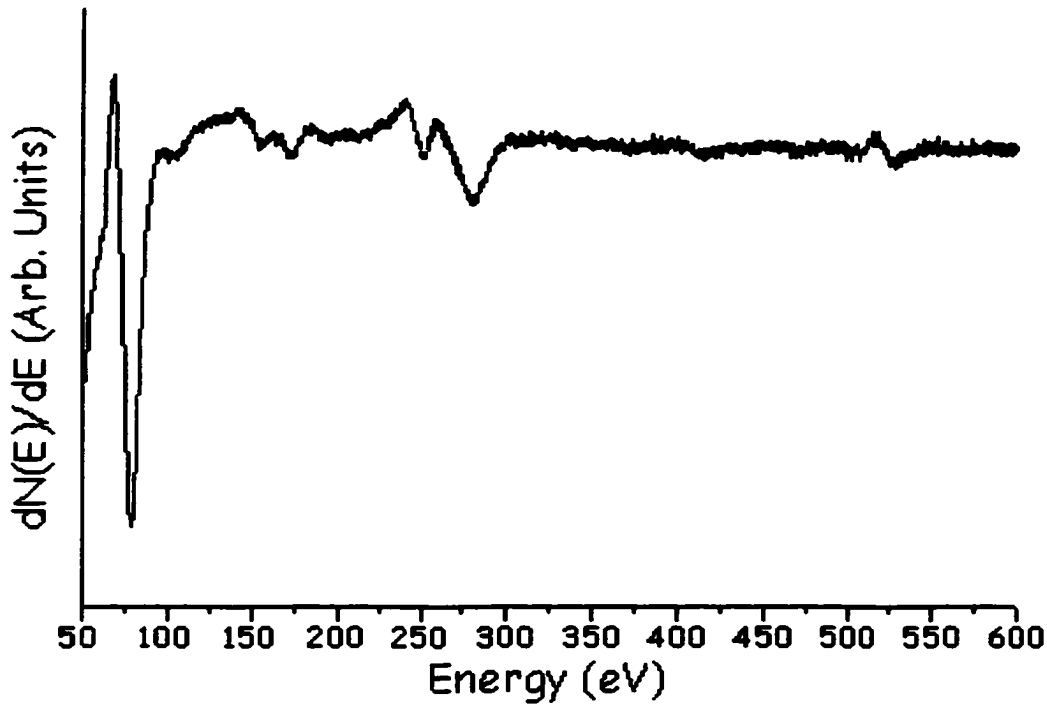

Figure 15. Auger spectra of bare Au(111). Major peaks are Au(74 eV), C(275 eV), and O(510 eV).

plotting the derivative versus energy yields very sharp spikes to measure at characteristic electron energies. Typically, the energy of the most negative part of a given spike is used as the reference[26]. The major peaks we observe are gold at 74 eV, carbon at 275 eV, and oxygen at 510 eV. The other peaks that are present in the spectra are all attributed to other gold transitions.

Instrumentation

The Auger electron spectrometer used in the lab is the Omicron Vacuumphysik GmbH Cylindrical Mirror Analyser (CMA) model CMA 100. A

Reproduced with permission of the copyright owner. Further reproduction prohibited without permission.

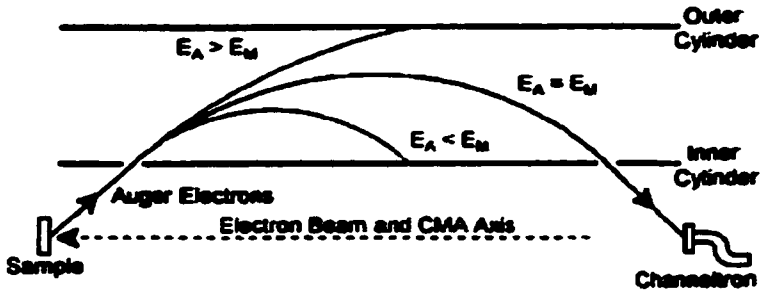

Figure 16. Schematic diagram of a cylindrical mirror analyser (*CMA*)[36].

3000 eV beam of electrons is fired at the surface and the Auger electrons are collected by a *CMA* and detector. The *CMA* is comprised of a pair of concentric metal cylinders which establish an electric field that guides the electrons with the desired energy toward the detector as shown in Figure 16[28]. This is achieved by biassing the outer cylinder positively with respect to the inner cylinder. Ramping the voltage on the outer cylinder (E_M) ramps the energy of the Auger electrons (E_A) that hit the detector. The detector is a channel electron multiplier (CEM). The CEM is a finely drawn tube of low electron binding energy material as shown in Figure 17. A high voltage is applied between the ends of the tube and the high resistivity of the material establishes a continuous voltage gradient[29]. Incident Auger electrons will trigger the emission of several secondary electrons which proceed further into the tube triggering more secondary electron emissions. CEMs can increase the electron

Reproduced with permission of the copyright owner. Further reproduction prohibited without permission.

current by a factor of 10^7.

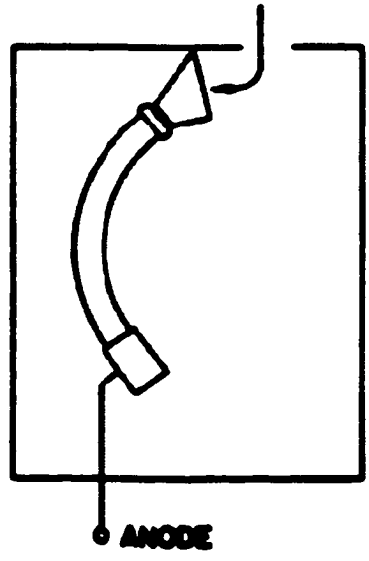

Figure 17. Channel electron multiplier[29].

Reproduced with permission of the copyright owner. Further reproduction prohibited without permission.

Sample Preparation

Reproduced with permission of the copyright owner. Further reproduction prohibited without permission.

Self-assembled monolayers were prepared by immersing flame annealed Au(111) surfaces in dilute (~1.0 mM) solutions of the thiols being investigated. The following sections overview the procedures involved in producing SAMs: gold films are made via gold evaporation onto atomically flat mica surfaces, domains with (111) termination are attained by flame annealing the gold film, and the polycrystalline gold films are modified with the desired thiol.

Gold Evaporation

Gold films were made by evaporating gold onto cleaved mica in high vacuum. Mica was used as the substrate because it is arranged in layers of atomically flat sheets which can be easily cleaved using adhesive tape to yield a clean, flat surface. The evaporating chamber was pumped to a base pressure of 8.0×10^{-6} Torr using a rotary vane roughing pump and a diffusion pump with a liquid nitrogen trap.

Once the base pressure was attained, the 1.0 mm gold wire was melted in a tungsten wire basket positioned 5 cm below the mica surface as shown in Figure 18. The mica was placed on a stage and held in place by a clipped glass slide which kept a heating filament in contact with the back of the mica. A thermocouple was used to monitor the temperature of the mica throughout the

Reproduced with permission of the copyright owner. Further reproduction prohibited without permission.

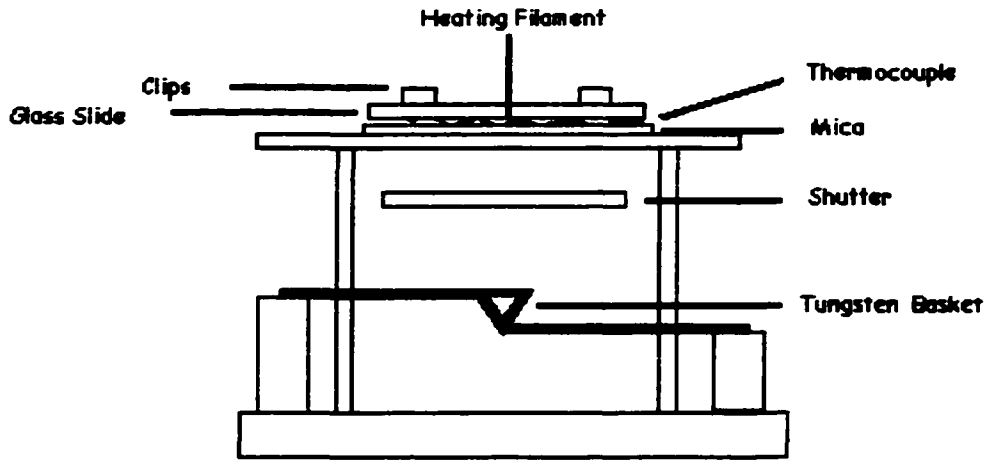

Figure 18. Evaporator set-up.

evaporation procedure. Prior to evaporation the mica was heated to 130°C using a 2.5 A current supplied by a DC constant current power source to expel water trapped between mica layers. Trapped water can destroy the film during the rapid heating of the flame annealing process.

Once the mica was sufficiently heated, the tungsten basket was heated by 16 A of current from a variac AC power supply. A shutter shielded the bare mica from evaporant until a stable gold flux was achieved. The mica was coated with gold for a period of five minutes. During this time the current from the power supply dropped up to 1 A depending on the quantity of gold wire that remained in the basket. The deposited film was allowed to cool under vacuum before it was removed for use.

Reproduced with permission of the copyright owner. Further reproduction prohibited without permission.

The evaporation process produced a 2 cm × 3 cm gold film that could be cut into smaller pieces (typically 0.5 cm × 0.8 cm) to fit into the sample vials for thiol modification and also the sample holder for the STM. Film thickness was measured using a fizeau plate interferometer[30] by measuring the fringe pattern produced. In order to measure the film thickness, a glass slide had to be used as the substrate since mica is riddled with large steps which can hinder the measurement. A molybdenum strip was placed between the slide and the basket to act as a mask during the first deposition. A second layer was deposited on top of the first to provide a reflecting surface for the interferometry. The fringe spacing and fringe offset were measured using the filar scale on the interferometer as shown in Figure 19 and the film thickness, t, was calculated

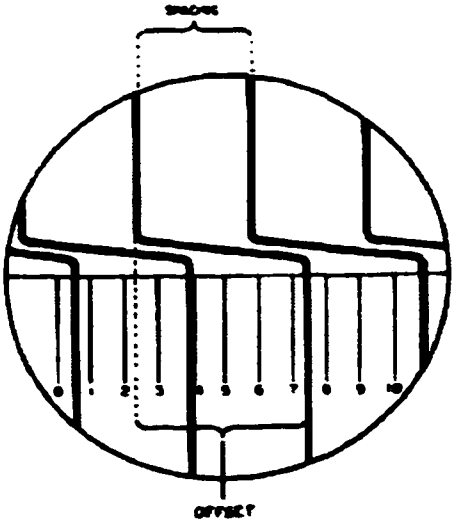

Figure 19. Fringe spacing and offset for typical step edge[30].

Reproduced with permission of the copyright owner. Further reproduction prohibited without permission.

using the expression[30]:

$$t = \frac{\text{Fringe Spacing}}{\text{Fringe Offset}} * 2946$$

Typical film thickness was measured to be ~5000 Å indicating a gold flux of ~15 Å/s.

Flame Annealing

Gold evaporation produces a thick film of gold that is very rough as shown in Figure 20a. The topography of the surface as seen with STM is very hilly with little evidence of crystalline terraces. The standard deviation about the mean height of the scan is 31.4 Å. The domain size ranges from about

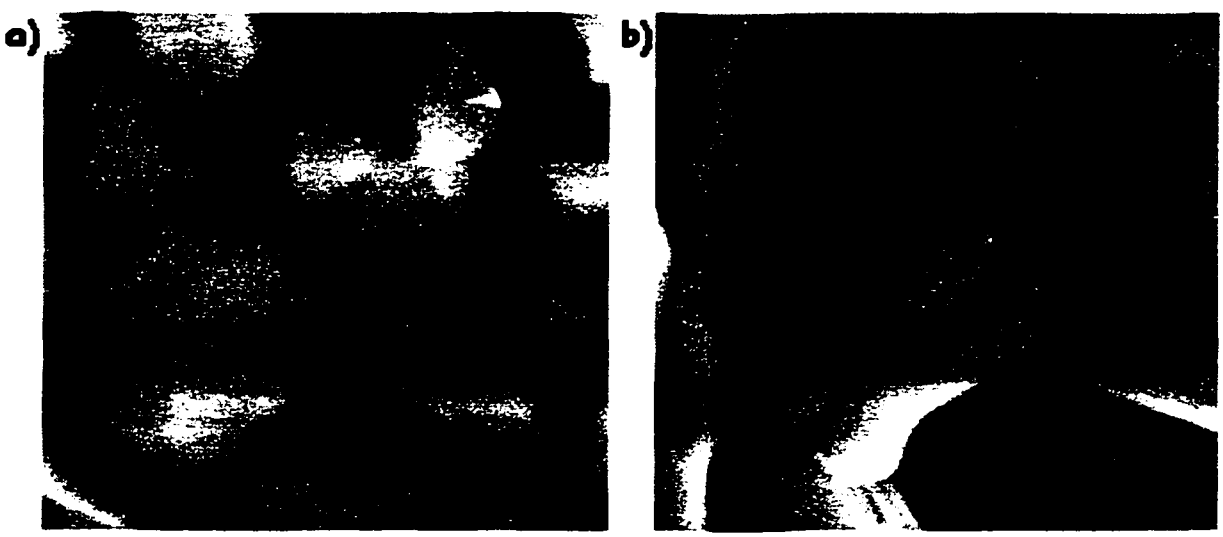

Figure 20. 5000 Å × 5000 Å STM images of a) pre- and b) post-annealed gold films. Tunneling conditions: a) +1.0 V and 0.86 nA and b) +1.0 V and 0.90 nA.

Reproduced with permission of the copyright owner. Further reproduction prohibited without permission.

400 Å × 400 Å to about 2000 Å × 2000 Å. Roughness varies from film to film but usually lies between 30 and 60 Å. In order to achieve large flat terraces with (111) termination, flame annealing is necessary[31].

The flame annealing procedure was carried out using a bunsen burner apparatus with a natural gas flame. The sample was quickly passed through the flame 1 cm above the bright blue tip. By the end of the annealing process, the edges of the mica had attained a reddish orange glow and the gold had been evaporated from the corners. After the sample was allowed to cool, the success of annealing was explored with STM as shown in Figure 20b. The standard deviation about the mean height of this scan was reduced to 8.8 Å and

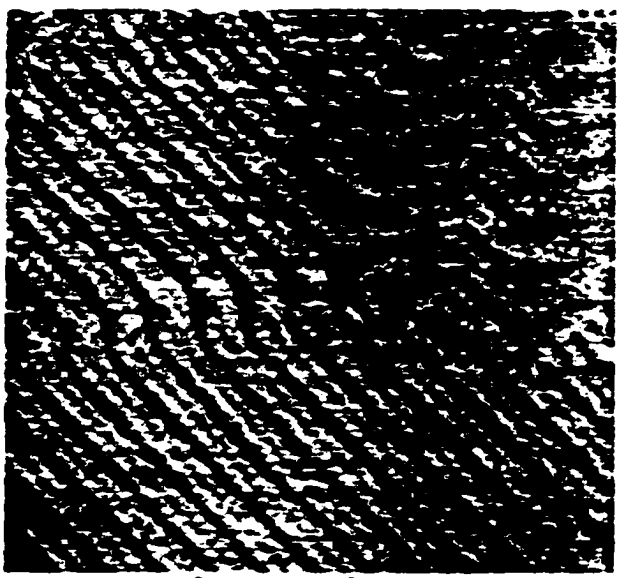

Figure 21. 1000 Å × 1000 Å STM image of the 23×√3 "herringbone" reconstruction of Au(111). Tunneling conditions: +0.02 V and 2.3 nA.

Reproduced with permission of the copyright owner. Further reproduction prohibited without permission.

the domain size greatly improved to 3000 Å × 3000 Å. Typically, surface roughness was reduced to 10-20 Å but more importantly the terraces exhibited hexagonal symmetry (120° between step edges) indicating that they were (111) terminated. The 23×√3 reconstruction was also verified by STM as shown in Figure 21. The parallel pairs of ridges were measured to be 0.20 Å high which is in close agreement with predicted values. The width of the pairs is ~60 Å which is also agrees with previous studies as discussed.

Thiol Modification

Once the termination of the gold films was verified and the terraces were large enough to perform sample measurements (500 Å × 500 Å), the films were incubated in thiol solution. The thiol solutions were prepared in HPLC grade ethanol at a concentration of 1.0 mM. This corresponds to an addition of 7.7 mg of DTT or 8.7 μL of octanethiol to 50 mL of ethanol. Films were modified at RT and at 60°C. For incubated films, the thiol solution was heated to 60°C prior to gold film introduction. The gold was then introduced into the heated thiol solution and remained at 60°C for the duration of the modification. After the modification, the samples were removed from solution and rinsed in copious amounts of ethanol to remove any unbound thiol.

Reproduced with permission of the copyright owner. Further reproduction prohibited without permission.

Modification Verification

Modification of the surface was verified using Auger electron spectroscopy and contact angle measurement. If Auger electron spectroscopy was used, the sample was mounted on a stainless steel sample holder with molybdenum clips and introduced into the (UHV) chamber via a load lock. The presence of thiol on the surface was verified by observing the S_{LMM} peak at

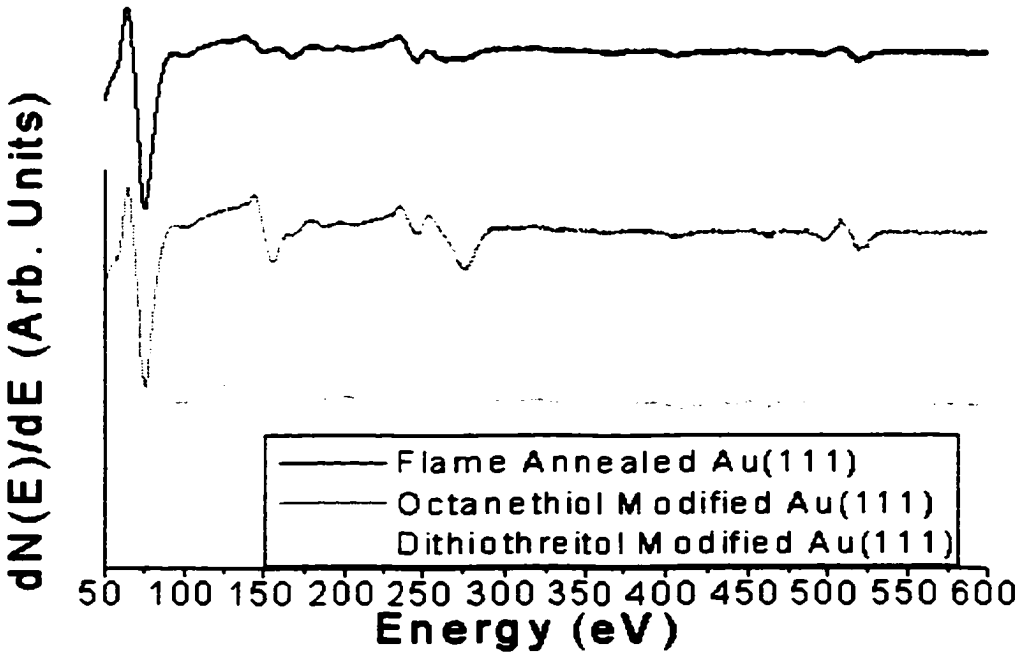

Figure 22. Auger spectra for bare gold, octanethiol, and dithiothreitol modified films. Major peaks are Au(74 eV), S(153 eV), C(275 eV), and O(510 eV).

Reproduced with permission of the copyright owner. Further reproduction prohibited without permission.

153 eV. Both octanethiol and DTT modified gold films exhibited a strong sulphur peak at an energy between 150 and 155 eV as shown in Figure 22. The ratio of S:Au was similar for the two films.

Contact angle measurements were made by placing a small water droplet onto the gold film. A photograph of the droplet was taken and the contact angle was measured. The contact angle was determined to be 50±7°, 98±2°, and 38±2° for bare gold, octanethiol and DTT respectively as shown in Figure 23. The higher contact angle for octanethiol can be attributed to the hydrophobic character of the methyl groups in the tail region of the molecule. The contact angle for DTT was lower due to the presence of hydrophilic hydroxyl groups.

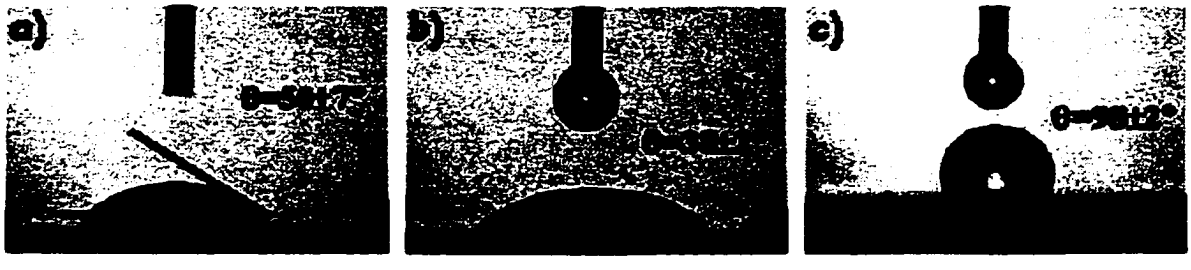

Figure 23. Contact angles for a) bare gold, b) a DTT modified surface, and c) a octanethiol modified surface.

Reproduced with permission of the copyright owner. Further reproduction prohibited without permission.

Results

Reproduced with permission of the copyright owner. Further reproduction prohibited without permission.

All STM images were obtained in constant current mode at RT. Large area scans were obtained at scan rates between 100 and 500 ms / line while molecular resolution images were obtained at scan rates between 10 and 100 ms / line.

Molecular Order

All Au(111) surfaces modified by octanethiol exhibited dense packed monolayers characteristic of n-alkanethiols. The c(4×2) superlattice of the (√3×√3)R30° pattern as shown in Figure 24 was observed regularly on the

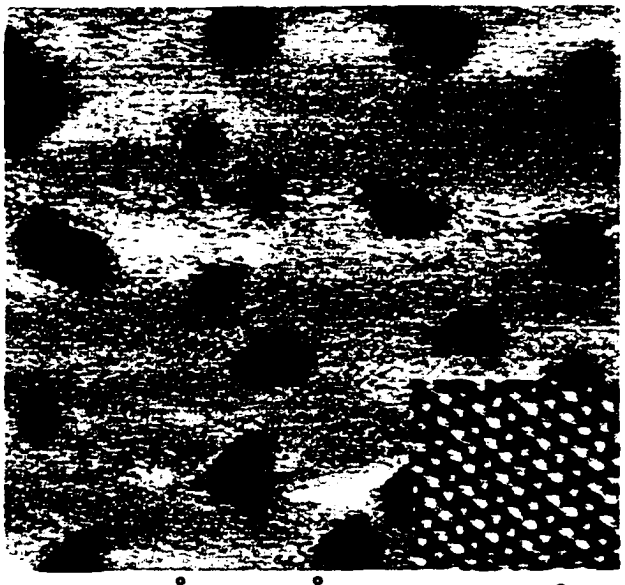

Figure 24. 500 Å × 500 Å STM image of a surface modified by 1.0 mM octanethiol in ethanol at 60°C for 4 hours. Inset: 50 Å × 50 Å STM image of c(4×2) superlattice of (√3×√3)R30° lattice. Tunneling conditions: +1.0 V and 1.04 nA and +1.0 V and 0.50 nA (inset).

Reproduced with permission of the copyright owner. Further reproduction prohibited without permission.

surfaces modified both at RT and 60°C. The periodicity was determined to be 5.2±0.2 Å which is close to √3 times the gold lattice spacing.

As was previously discussed, the STM maps out contours of constant electron density near the Fermi level of the sample at the position of the tip. For simple metals, the conduction band is half full so there is a high density of states near the Fermi level. Once the conducting surface is covered by an organic monolayer, direct interpretation of STM images becomes more difficult. Since methyl groups are poor conductors, the majority of the tunnel current is expected to flow between the tip and the sulphur head group.

A study of the self-assembly of mixed n-alkanethiols of differing chain lengths (n=10 and n=12) revealed two distinct height levels[32]. While the effect of adsorbed molecules on the tunnel barrier is not well understood, the following argument was proposed to explain the observed height difference of the two molecules. The tunnel barrier between the sample and the tip can be subdivided into two regions, the vacuum, or air barrier, and the film barrier of insulating alkyl tails as shown in Figure 25. Each region will have a different inverse decay length. Since the tunnel impedance is held uniform during constant current imaging, the change in film barrier thickness due to longer

Reproduced with permission of the copyright owner. Further reproduction prohibited without permission.

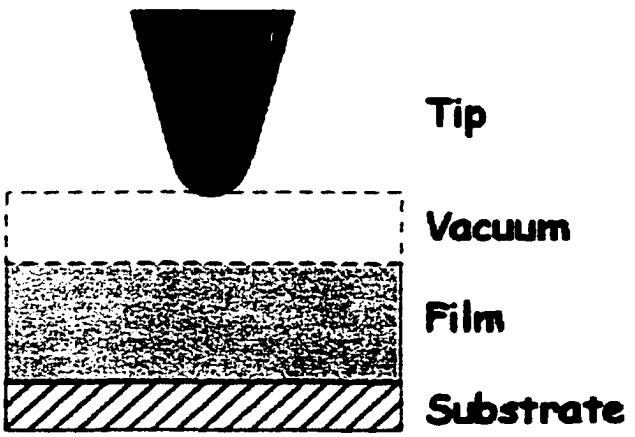

Figure 25. Model of tunnel junction for a SAM[32].

alkyl chains has to be compensated by a change in vacuum barrier thickness and hence the tip height changes. Given the insulating nature of alkyl chains it is possible to operate the STM with the tip inside the thiol layer, however molecular resolution requires that the tip lie outside the molecular layer. For longer thiols, it is necessary to scan at a very low tunnel current to raise the tunnel impedance to 10s or 100s of GΩ to keep the tip outside the SAM.

For octanethiol modified films, stripes were observable under 1.0 V and 1.0 nA tunnel conditions giving a tunnel impedance of 1.0 GΩ. To observe individual octanethiol molecules the tunnel current had to be lowered to 0.5 nA to raise the tunnel impedance suggesting that a 1.0 GΩ tunnel impedance does not keep the tip outside the octanethiol monolayer. No bias dependence was observed for this system.

Reproduced with permission of the copyright owner. Further reproduction prohibited without permission.

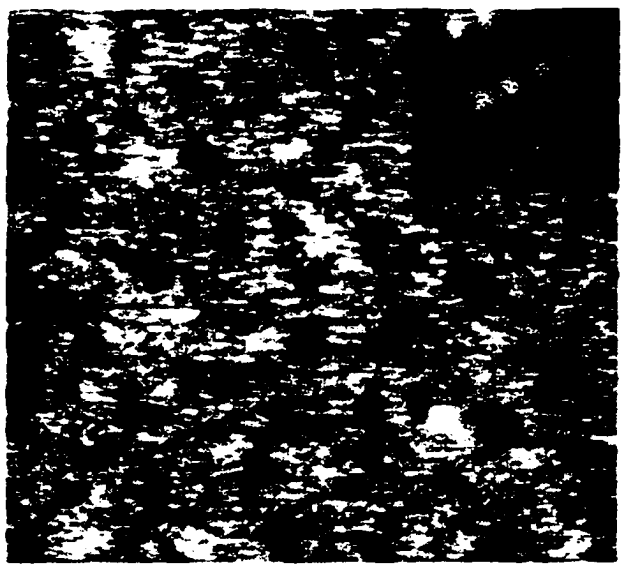

Figure 26. 500 Å × 500 Å STM image of a surface modified by 1.0 mM DTT in ethanol at 60°C for 3 hours. Inset: 30 Å × 30 Å STM molecular resolution image of a surface modified by DTT in ethanol at 60°C for 12 hours. Tunneling conditions: -0.87 V and 0.49 nA and -0.67 V and 0.49 nA (inset).

Au(111) surfaces modified by dithiothreitol (DTT) at 60°C exhibited small domains of molecular order, however, the majority of the surface appeared to be disordered as shown in Figure 26. In the ordered region, the lattice spacing was ~5 Å along one direction and 10-15 Å along the other direction. This unit cell ($2\sqrt{3}\times\sqrt{3}$) is larger than the close packed n-alkanethiol unit cell ($\sqrt{3}\times\sqrt{3}$) suggesting that DTT does not pack as densely.

In order to observe individual molecules the tunnel current had to be

Reproduced with permission of the copyright owner. Further reproduction prohibited without permission.

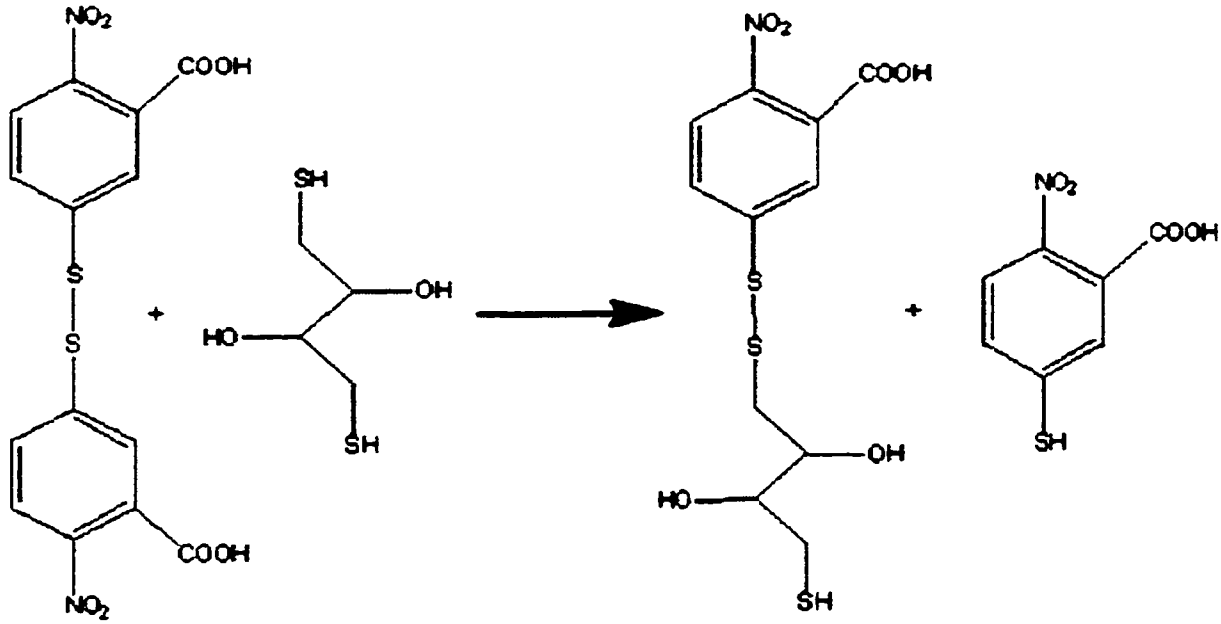

Figure 27. Example of chemical reaction between DTNB and free DTT.

reduced to 0.5 nA and the voltage had to be reduced to ~0.7 V. We were only successful in obtaining molecular images under negative sample bias conditions. At this time, the nature of the bias dependence remains uninvestigated.

Au-DTT Binding

One question that arises when studying dithiols is whether or not each molecule binds to the surface via one or two Au-S bonds? To further address this question, Ellman's reagent or 5-5'-dithiobis(2-nitrobenzoic acid) (DTNB) was used to detect free thiol on the surface. Surfaces with exposed sulphydryl groups react with DTNB to form a complex and liberate 5-thio(2-nitrobenzoic

Reproduced with permission of the copyright owner. Further reproduction prohibited without permission.

acid) (TNB) as shown in Figure 27[33]. In free solutions, TNB is strongly coloured (412 nm) and can be detected using UV/Visible spectroscopy. Unfortunately, the amount of TNB that would be liberated by a reaction at the surface would be undetectable by UV/Visible spectroscopy. To overcome this problem, the samples were exposed to DTNB and then introduced into the UHV chamber were AES was used to detect the presence of nitrogen on the surface. The N_{KLL} peak at 389 eV is not observed on bare or thiol modified Au(111) films so its presence on films exposed to DTNB would suggest the presence of TNB bound to the surface.

Bare Au(111) films treated with DTNB exhibited a small nitrogen peak at 389 eV as shown in Figure 28. Comparison of sensitivity factors[28] of sulphur (4.7575) and nitrogen (1.2184) indicate that nitrogen was present in similar quantities to sulphur suggesting that there was a complete layer of TNB on the surface. Exposure of octanethiol and dithiothreitol modified surfaces to DTNB resulted in no observable nitrogen peak suggesting that all sulphur present at the surface is bound to the gold. The size of the carbon and oxygen peaks cannot be used to obtain information about the surface because the surface is generally coated with carbon dioxide in varying amounts.

Reproduced with permission of the copyright owner. Further reproduction prohibited without permission.

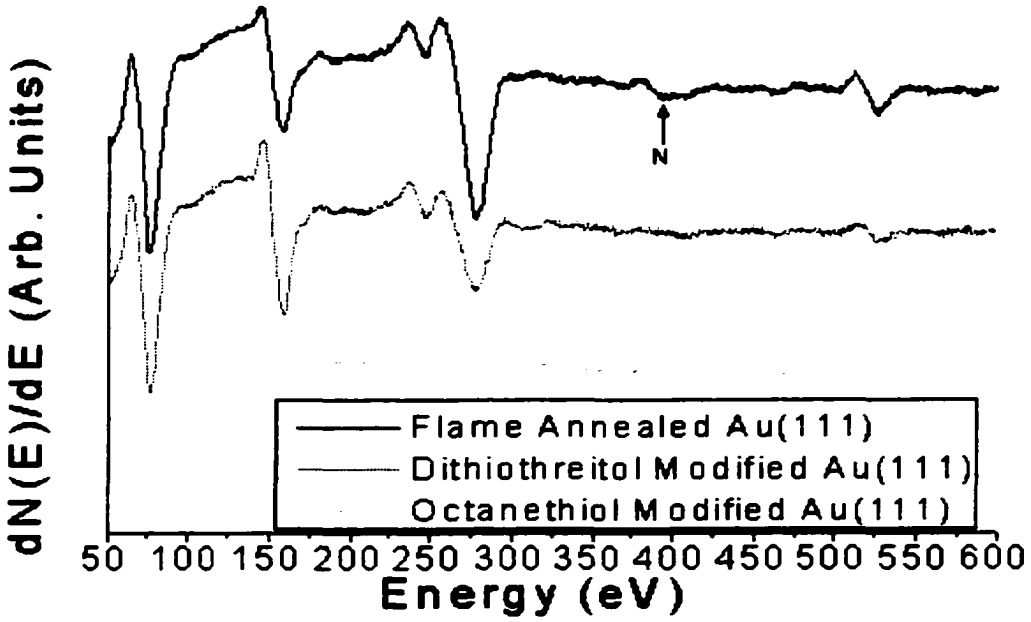

Figure 28. *Auger spectra of flame annealed gold and dithiothreitol and octanethiol modified surfaces exposed to DTNB for 15 minutes. The spectra are normalized with respect to the Au peak. Major peaks are Au(74 eV), S(153 eV), C(275 eV), N(389 eV) as indicated, and O(510 eV).*

Previous Auger results (Figure 22) of octanethiol and DTT modified films suggest a similar areal density of sulphur on the gold. Results with DTNB indicate that both sulphur atoms bind to the surface. Based on these results and the observed ($2\sqrt{3}\times\sqrt{3}$) unit cell observed in STM (Figure 26), we propose the

Reproduced with permission of the copyright owner. Further reproduction prohibited without permission.

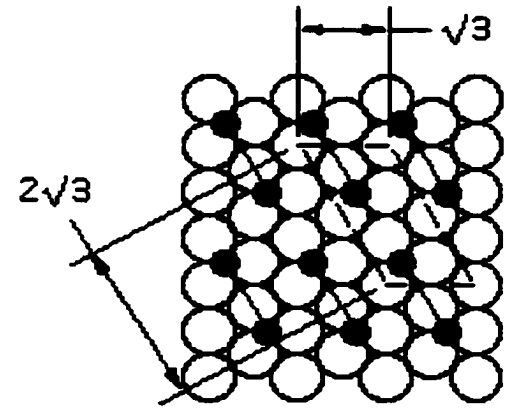

Figure 29. Structural model for DTT on Au(111).

structural model shown in Figure 29. Conformational analysis of DTT suggests that having both S oriented in the same direction (ie. down) and spaced 5 Å apart is a low energy state of the molecule[34]. It should be noted that the molecule is comprised of single bonds which exhibit free rotation. In this model, the sulphur atoms are still densely packed, however, there are two sulphur atoms per molecule so the unit cell becomes larger. This unit cell has a molecular area of 49.8 $Å^2$ which is consistent with the spacing observed.

Pitting

All Au(111) surfaces modified by octanethiol exhibited pitting characteristic of dense packed n-alkanethiols at both RT and 60°C. Au(111) surfaces modified by DTT at 60°C exhibited pitting similar to that observed on octanethiol SAMs. Pits were too small to be resolved if the incubation time was

Reproduced with permission of the copyright owner. Further reproduction prohibited without permission.

less than 90 minutes. As well, pits could not be resolved on surfaces modified at RT regardless of the modification time.

The single step height depressions that are observed in SAM systems were originally believed to arise due to chemical etching of the surface by the thiol in solution[35]. Evidence for this was discovered when gold particles where observed in solution after modification. As the phenomenon of pitting became more thoroughly investigated, it was discovered that pits formed during gas phase deposition as well as liquid phase deposition.

Studies of initial SAM formation revealed that the herringbone reconstruction relaxes as a result of thiol adsorption[11]. The extra gold atoms present in the reconstructed layer are displaced onto the surface layer upon relaxation where they quickly migrate towards a step edge. It is believed that a second gold atom per unit cell is also ejected and subsequently migrates towards the step edge. This leaves behind one vacancy per unit cell. The vacancies in the surface gold layer cannot diffuse as quickly as the adatoms and, as the thiol adsorption continues, vacancies begin to migrate and nucleate vacancy islands as shown in Figure 30.

In order to make a comparison between the pitting characteristics of

Reproduced with permission of the copyright owner. Further reproduction prohibited without permission.

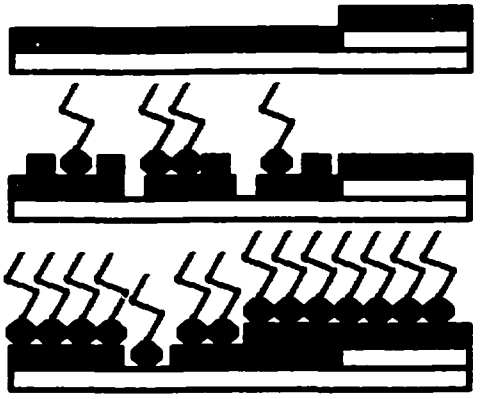

Figure 30. Diagram depicting Au(111) surface relaxation and Au adatom (black squares) and vacancy (white squares) migration. White layers represent bulk gold layers (σ=1.000) while gray layers represent reconstructed gold layers (σ=1.044)[11].

DTT and octanethiol, the time evolution of fractional pit surface area and mean pit radius was investigated. The pit surface area and number density was measured using Image SXM for the MacIntosh platform[36]. The raw data was loaded into the software and modified using the program's image editing macros.

First, a linear and quadratic compensation was performed to account for slope changes from line to line in the scan. Next, a 7×7 Gaussian filter as shown in Figure 31 was applied to smooth the surface features. The enhance contrast macro was then used to maximize the pixel resolution of the image. A threshold was performed to convert pixels below 40 % of an atomic layer to black while those above the threshold were set to white. The fractional

Reproduced with permission of the copyright owner. Further reproduction prohibited without permission.

1 1 2 2 2 1 1
1 2 2 4 2 2 1
2 2 4 8 4 2 2
2 4 8 16 8 4 2
2 2 4 8 4 2 2
1 2 2 4 2 2 1
1 1 2 2 2 1 1

Figure 31. 7×7 Gaussian filter used to smooth STM data.

coverage was determined by comparing the number of black pixels to the number of white pixels. A particle counting macro was then used to count the number of pits with surface area greater than 100 Å^2. The 100 Å^2 cutoff was used to eliminate spurious statistics arising from noise in the data. The mean pit radius was calculated using the following equation assuming the circular pits:

$$\bar{r} = \sqrt{\frac{1}{\pi}\frac{FractionalArea \times ImageArea}{NumberOfPits}}$$

Fractional Pit Area

In both systems under investigation, the pits occupied 5-10 % of the total surface area of the film as shown in Figure 32. The fluctuations in fractional area can be attributed to changes in tip geometry as the tip was often recut prior to each sample imaging. There was no clear trend observed as the results fluctuated over this range. Incubation time does not seem to have

Reproduced with permission of the copyright owner. Further reproduction prohibited without permission.

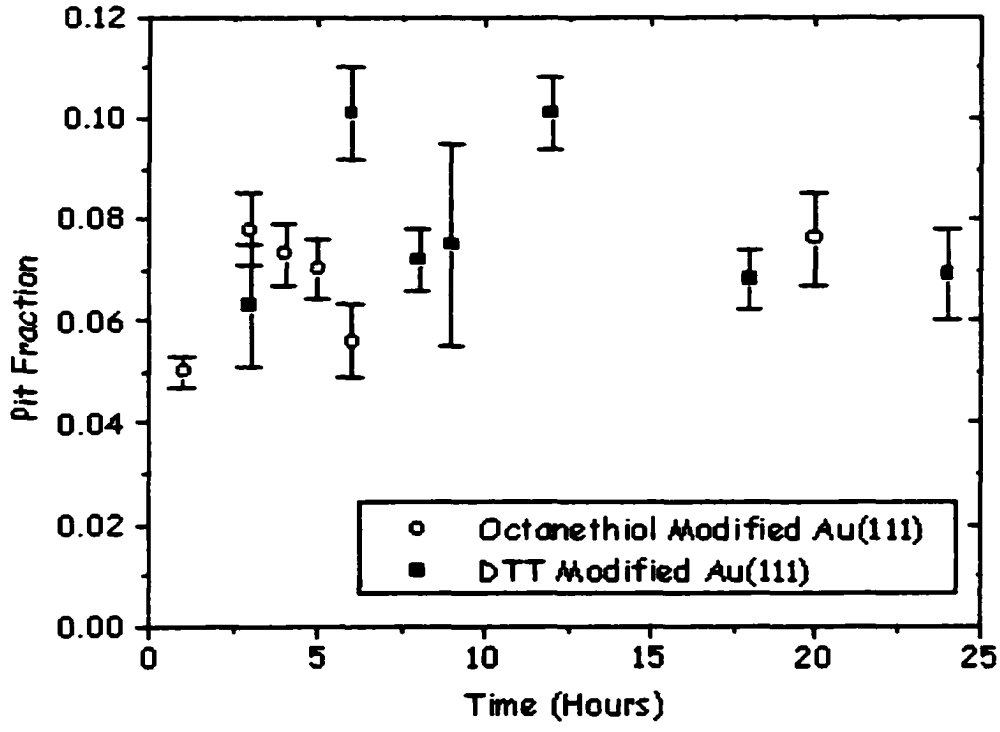

Figure 32. Graph of pit fraction versus modification time for octanethiol and DTT modified surfaces incubated at 60°C. Error bars quantify inter- and intra-sample variations.

an effect on the fractional coverage of pits beyond one hour of modification consistent with previous studies[37] indicating that pit formation reaches equilibrium before one hour of modification time. It should be re-emphasized that pits were not resolvable on DTT modified samples incubated for 90 minutes or less whereas octanethiol modified samples had resolvable pits at one hour. This result suggests that DTT modified surfaces take longer to reach equilibrium.

Reproduced with permission of the copyright owner. Further reproduction prohibited without permission.

The consistency of the pit fractional coverage for both octanethiol and DTT modified films suggests a common mechanism for pit formation. The close agreement between the observed results and previous studies[11] suggest that pit formation is independent of the tail groups of the thiols and that simply the presence of thiol triggers pitting.

Another interesting observation of the surfaces resulting from thiol modification was the observation of evidence for mass transport of terraces. According to the herringbone relaxation model, terraces should expand as a result of adatom migration to ascending step edges as shown in Figure 30.

Figure 33. 5000 Å × 5000 Å STM image of a surface modified by 1.0 mM octanethiol in ethanol at 60°C for 20 hours showing pinning sites. Tunneling conditions: -1.0 V and 0.98 nA.

Reproduced with permission of the copyright owner. Further reproduction prohibited without permission.

Octanethiol modified surfaces were characterized by terraces that grew larger around pinning sites as shown in Figure 33. Pinning sites arise as terraces move through local defects or impurities in the crystal structure. The defect or impurity prevents local crystal growth as the rest of the terrace expands. Notice the higher terraces wrap around the pinning sites suggesting that the terraces are advancing.

In contrast, DTT modified surfaces exhibit evidence of terrace recession as shown in Figure 34. Here the terraces appear to be pulling away from the pinning sites. It is also interesting to note that pinning sites are

Figure 34. 5000 Å × 5000 Å STM image of a surface modified by 1.0 mM DTT in ethanol at 60°C for 1 hour showing pinning sites. Tunneling conditions: -1.0 V and 0.52 nA.

Reproduced with permission of the copyright owner. Further reproduction prohibited without permission.

observed before pits are resolvable. This phenomenon cannot be explained in terms of the pit formation theory but rather suggest that the surface is being eroded by the modification process.

Mean Pit Radius

It has been observed by a number of groups that pits undergo a ripening process over time whereby larger pits grow at the expense of smaller pits[38]. This process, often referred to as Ostwald ripening, is affected by the evaporation rate of vacancies from the pit edges and the diffusion rate of vacancies from high curvature step edges to lower curvature step edges. Pit ripening should obey a power law relationship ($r \propto t^n$) where n=0.33 if diffusion is the rate limiting step and n=0.50 if evaporation is the rate limiting step. Studies of butanethiol on Au(111) at RT determined that pit ripening is evaporation limited[39].

The mean pit radius was measured for all octanethiol and DTT samples incubated over a range of times from one to twenty-four hours as shown in Figure 35. Both systems seemed to reach a similar saturation mean pit radius between 18-20 Å consistent with similar studies[37]. However, while octanethiol modified films are close to this saturation level at one hour it seems that DTT

Reproduced with permission of the copyright owner. Further reproduction prohibited without permission.

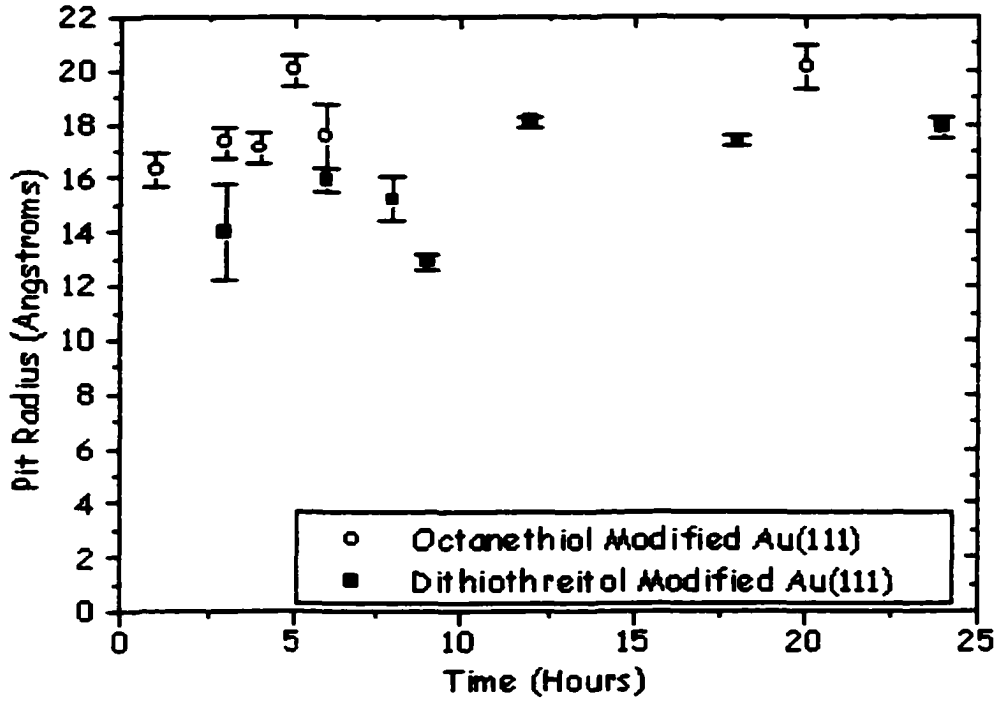

Figure 35. Pit radius versus modification time for octanethiol and DTT modified surfaces incubated at 60°C. Error bars quantify inter- and intra-sample variations.

modified films do not reach that level for several hours. Samples incubated for 90 minutes exhibit pits shallower than 2.5 Å. These pits are too small for the tip to image before it encounters the other side. It should also be noted that pits are not resolvable on films modified by DTT at RT regardless of the incubation time (up to several days) suggesting that increased temperature is required to ripen the pits on DTT modified SAMs. The increased thermal energy may be required to facilitate evaporation from step edges since there

Reproduced with permission of the copyright owner. Further reproduction prohibited without permission.

are two Au-S bonds to overcome.

Preliminary investigations of octanethiol modified films at RT suggest that the equilibrium mean pit radius decreases with decreasing temperature consistent with previous studies[37]. Samples modified for 46 hours at RT exhibited a mean pit radius of ~11 Å. This result is expected since evaporation is a thermodynamic phenomenon.

At first glance, the data shown in Figure 35 does not appear to obey the power law for Ostwald ripening. At 60°C, it is most probable that the transition from unresolvable pits at low incubation times to the saturation pit radius occurred too quickly to be observed in our measurements. There is also a dependence on temperature as is evident from the smaller saturation pit radius for octanethiol modified at RT.

Reproduced with permission of the copyright owner. Further reproduction prohibited without permission.

Summary

Reproduced with permission of the copyright owner. Further reproduction prohibited without permission.

We compared the properties of dithiothreitol self-assembled monolayers to octanethiol self-assembled monolayers. The results observed for octanethiol modified films were consistent with previous studies. For the first time, STM images of dithiothreitol were obtained. Molecular resolution images along with Auger results were used to determine the structure of the film.

The octanethiol modified films exhibited properties characteristic of n-alkanethiol SAMs as expected. The c(4×2) superlattice of the (√3×√3)R30° SAM was observed with the appropriate lattice spacings (5.2±0.2 Å). Numerous pits were observed with the characteristic depth of 2.5 Å consistent with the height of a single gold step.

The fraction of the surface covered by pits always fell between 0.05-0.10 regardless of incubation time. These results are in agreement with previous studies based on relaxation of the gold surface reconstruction[11]. The mean pit radius seemed to quickly reach an equilibrium value of ~19 Å. Samples modified at RT reached an equilibrium value of ~11 Å. Evidence for mass transport of terraces was also observed suggesting that the adatoms liberated by the relaxation of the herringbone reconstruction migrate towards step edges resulting in the growth of the terrace consistent with the theory of pit

Reproduced with permission of the copyright owner. Further reproduction prohibited without permission.

formation.

Dithiothreitol modified films exhibited many properties similar to those observed in n-alkanethiol SAMs with a few exceptions. The films did not exhibit long range order as observed for octanethiol and the order that was observed suggested that DTT does not form a densely packed monolayer. Pits were observed to be 2.5 Å deep for films modified at 60°C however, pits were unresolvable when the gold surface was modified at RT. Preliminary studies with Ellman's reagent (DTNB) suggest that DTT binds to the gold surface via two Au-S bonds. The structural model proposed for DTT is $(2\sqrt{3}\times\sqrt{3})$.

The fractional pit coverage was also observed to lie in the range of 0.05-0.10 and the mean pit radius appeared to reach the same equilibrium value of ~19 Å. The data suggest that the origin of pitting is similar in both systems. Pits on DTT modified films take longer to reach equilibrium than was observed for octanethiol SAMs. There was also evidence of mass transport of terraces however, contrary to octanethiol modified films, DTT modified films exhibit receding terraces. This phenomenon can not be explained using the theory of pit formation and is attributed to some sort of etching mechanism.

Reproduced with permission of the copyright owner. Further reproduction prohibited without permission.

Future Considerations

At this time, it is unclear how the DTT modified films order with respect to the underlying Au(111) substrate. Observing the registry of the DTT SAM would help determine the DTT packing structure.

In-situ STM investigations could observe the early stages of modification in the DTT system. Probing the initial pit formation and subsequent pit dynamics would help answer questions about the nature of the binding of the DTT to the surface and also about the mobility of the SAM.

The observation of terraces receding in DTT modified films can not be explained using current theories about SAM formation and evolution. In-situ STM investigations need to be performed to observe the mass transport of terraces during modification.

The use of DTNB provided insight into the nature of the binding of the DTT SAM. However, nitrogen is a poor choice for a marker since it is very close to a secondary peak of gold. Another marker species with a stronger Auger signal , chlorine for example, would be a better choice.

The bias dependence of stable molecular imaging for DTT SAMs should be more thoroughly investigated as it may shed some light on how the DTT

Reproduced with permission of the copyright owner. Further reproduction prohibited without permission.

presents itself at the surface.

Reproduced with permission of the copyright owner. Further reproduction prohibited without permission.

Literature Cited

Reproduced with permission of the copyright owner. Further reproduction prohibited without permission.

1. G. E. Poirier. Characterization of Organosulfur Molecular Monolayers on Au(111) using Scanning Tunneling Microscopy. Chem. Rev., 97, 1117-1127 (1997).

2. E. Schmidt, W. Schurig, and W. Sellschopp. Tech. Mech. Thermodyn., 1, 53 (1930). (Cited in Reference 1)

3. L. C. F. Blackman, and M. J. S. Dewar. J. Chem. Soc., 162 (1957). (Cited in Reference 1)

4. R. G. Nuzzo, and D. L. Allara. Adsorption of Bifunctional Organic Disulfides on Gold Surfaces. J. Am. Chem. Soc., 105, 4481 (1983).

5. E. Huang, F. Zhou, and L. Deng. Studies of Surface Coverage and Orientation of DNA Molecules Immobilized onto Preformed Alkanethiol Self-Assembled Monolayers. Langmuir, 16, 3272-3280 (2000).

6. E. Boubour, and R. B. Lennox. Potential-Induced Defects in n-Alkanethiol Self-Assembled Monolayers Monitored by Impedance Spectroscopy. J. Chem. Phys. B, 104, 9004-9010 (2000).

7. L. A. Bumm, J. J. Arnold, M. T. Cygan, T. D. Dunbar, T. P. Burgin, L. Jones II, D. L. Allara, J. M. Tour, and P. S. Weiss. Are Single Molecular Wires Conducting?. Science, 271, 1705-1707 (1996).

8. W. T. Müller, D. L. Klein, T. Lee, J. Clarke, P. L. McEuen, and P. G. Schultz. A Strategy for the Chemical Synthesis of Nanostructures. Science, 268, 272-273 (1995).

9. A. Ulman. Formation and Structure of Self-Assembled Monolayers. Chem. Rev., 96, 1533-1554 (1996).

10. C. Kittel. 1996. Introduction to Solid State Physics: Seventh Edition. John Wiley and Sons, Inc., New York, USA. 673 pp. (Ch. 1)

11. G. E. Poirier. Mechanism of Formation of Au Vacancy Islands in Alkanethiol Monolayers on Au(111). Langmuir, 13, 2019-2026 (1997).

Reproduced with permission of the copyright owner. Further reproduction prohibited without permission.

12. C. Wöll, S. Chiang, R. J. Wilson, and P. H. Lippel. Determination of Atom Positions at Stacking-Fault Dislocations on Au(111) by Scanning Tunneling Microscopy. Phys. Rev. B., 39, 7988-7991 (1989).

13. C. A. Widrig, C. A. Alves, and M. D. Porter. Scanning Tunneling Microscopy of Ethanethiolate and n-Octadecanethiolate Monolayers Spontaneously Adsorbed at Gold Surfaces. J. Am. Chem. Soc., 113, 2805-2810 (1991).

14. R. G. Nuzzo, E. M. Korenic, and L. H. Dubois. Studies of the Temperature Dependent Phase Behaviour of Long Chain n-Alkyl Thiol Monolayers on Gold. J. Chem. Phys., 93, 767-773 (1990).

15. G. E. Poirier, and M. J. Tarlov. The c(4×2) Superlattice of n-Alkanethiol Monolayers Self-Assembled on Au(111). Langmuir, 10, 2853-2856 (1994).

16. J. Noh and M. Hara. Phase Transitions of Alkanethiol Self-Assembled Monolayers on Au(111): Coverage, Temperature, and Time Dependence. 11th International Conference on Scanning Tunneling Microscopy / Spectroscopy and Related Techniques. Vancouver, Canada (2001).

17. J. Voets, J. W. Gerritsen, R. F. P. Grimbergen, and H. van Kempen. Chain-Length Dependent Structure of Alkanethiols from dimers on Au(111). Surf. Sci., 399, 316-323 (1998).

18. E. Delamarche, B. Michel, H. Kang, and C. Gerber. Thermal Stability of Self-Assembled Monolayers. Langmuir, 10, 4103-4108 (1994).

19. R. Wiesendanger. 1994. Scanning Probe Microscopy and Spectroscopy: Methods and Applications. Cambridge University Press, Cambridge, UK. 637 pp.

20. J. A. Stroscio, and W. J. Kaiser. 1993. Scanning Tunneling Microscopy. Academic Press, Inc., San Diego, USA. 459 pp.

21. A. Beiser. 1995. Concepts of Modern Physics: Fifth Edition. McGraw-Hill, Inc., New York, USA. 534 pp. (Ch. 5)

Reproduced with permission of the copyright owner. Further reproduction prohibited without permission.

22. R. L. Strauss. 1968. Quantum Mechanics: An Introduction. Prentice-Hall Inc., New Jersey, USA. 192 pp.

23. J. Tersoff and D. R. Hamann. Theory and Application for the Scanning Tunneling Microscope. Phys. Rev. Lett., 50, 1998-2001 (1983).

24. RHK Technology, Inc. 1994. PPC 100: Installation Guide. Rochester Hills, USA.

25. J. A. Delchar, and D. Woodruff. 1994. Cambridge Solid State Science Series: Modern Techniques of Surface Science: Second Edition. Cambridge University Press, Cambridge, UK. 586 pp.

26. R. L. Park, and M. G. Lagally. 1985. Methods of Experimental Physics: Volume 22. Solid State Physics: Surfaces. Academic Press, Inc., Orlando, USA. 543 pp.

27. M. Prutton. 1994. Introduction to Surface Physics. Oxford University Press, New York, USA. 196 pp.

28. C. L. Hedberg. 1995. Handbook of Auger Electron Spectroscopy: Third Edition. Physical Electronics, Inc., Eden Prairie, USA. 405 pp.

29. J. F. O'Hanlon. 1989. A User's Guide to Vacuum Technology: Second Edition. John Wiley and Sons, New York, USA. 481 pp.

30. Varian. 1966. Å-Scope Interferometer Model Nos. 980-4000/4006 Instruction Manual. Palo Alto, USA.

31. M. H. Dishner, M. M. Ivey, S. Gorer, J. C. Hemminger, and F. J. Feher. Preparation of Gold Thin Films by Epitaxial Growth on Mica and the Effect of Flame Annealing. J. Vac. Sci. Tech. A, 16, 3295-3300 (1998).

32. L. A. Bumm, J. J. Arnold, T. D. Dunbar, D. L. Allara, and P. S. Weiss. Electron Transfer Through Organic Molecules. J. Phys. Chem. B, 103, 8122-8127 (1999).

33. G. L. Ellman. Tissue Sulfhydryl Groups. Arch. Biochem. Biophys., 82, 70-77 (1959).

Reproduced with permission of the copyright owner. Further reproduction prohibited without permission.

34. Personal communication, J. T. Banks, Acadia University, 2001.

35. C. Schönenberger, J. A. M. Sondag-Houethorst, J. Jorritsma, and L. G. J. Fokkink. What Are the "Holes" in Self-Assembled Monolayers of Alkanethiols on Gold?. Langmuir, 10, 611-614 (1994).

36. National Institute of Health (NIH), USA Image v1.62 with Extensions for Scanning Microscopy (Image SXM) v1.66 by Steve Barrett, Surface Science Research Centre, University of Liverpool, Liverpool, UK.

37. R. Yamada, H. Wano, and K. Uosaki. Effect of Temperature on Structure of the Self-Assembled Monolayer of Decanethiol on Au(111) Surface. Langmuir, 16, 5523-5525 (2000).

38. O. Cavalleri, A. Hirstein, and K. Kern. Ostwald Ripening of Vacancy Islands at Thiol Covered Au(111). Surf. Sci., 340, 960-964 (1995).

39. G. E. Poirier and M. J. Tarlov. Molecular Ordering and Gold Migration Observed in Butanethiol Self-Assembled Monolayers Using Scanning Tunneling Microscopy. J. Phys. Chem., 99, 10966-10970 (1995).

Reproduced with permission of the copyright owner. Further reproduction prohibited without permission.